J. Fluid Mech. (1992), *vol.* 245, *pp.* 449–483

Multiple equilibria in thermosolutal convection due to salt-flux boundary conditions

By CHARLES QUON† AND MICHAEL GHIL‡

Climate Dynamics Center and Department of Atmospheric Sciences, University of California,
Los Angeles, CA 90024-1565, USA

(Received 1 December 1991 and in revised form 20 April 1992)

Long-term variability in the ocean's thermohaline circulation has attracted considerable attention recently in the context of past and future climate change. Drastic circulation changes are documented in paleoceanographic data and have been simulated by general circulation models of the ocean. The mechanism of spontaneous, abrupt changes in thermohaline circulation is studied here in an idealized context, using a two-dimensional Boussinesq fluid in a rectangular container, over 5 decades of Rayleigh number.

When such a fluid is forced with a specified distribution of temperature and salinity at the surface – symmetric about a vertical axis – it attains a stable two-cell circulation, with the same symmetry. On the other hand, replacement of the specified salinity surface condition with an appropriate symmetric salt-flux condition leads to loss of stability of the symmetric circulation and gives rise to a new, asymmetric state. The extent of asymmetry depends on the magnitude of the thermal Rayleigh number, *Ra*, and on the strength of the salinity flux, γ. An approximate stability curve in the γ-*Ra* space, dividing the symmetric from the asymmetric states, is obtained numerically, and the entire range of asymmetric flows, from very slight dominance of one cell to its complete annihilation of the other cell, is explored. The physical mechanism of the pitchfork bifurcation from symmetric to asymmetric states is outlined. The effects of three other parameters of the problem are also discussed, along with implications of our results for glaciation cycles of the geological past and for interdecadal oscillations of the present ocean–atmosphere system.

1. Introduction and motivation

The problem of thermal convection in an enclosed fluid is mathematically well known and physically interesting in both stationary and rotating frames of reference (Batchelor 1954; Gill 1966; McIntyre 1968; Daniels & Stewartson 1977, 1978; Quon 1980, 1983; and others). However, thermosolutal convection in a fluid with density dependent on both heat and salt content is a far more difficult and far less completely explored problem (Turner 1973); such a fluid is sometimes said to have two components, although it has uniform physics (one phase) and chemistry (one constituent).

In the last few years, physical oceanographers have discovered from Ocean

---

† Permanent address: Department of Fisheries & Oceans, Bedford Institute of Oceanography, Dartmouth, Nova Scotia, Canada.

‡ Also Institute of Geophysics and Planetary Physics, UCLA, USA.

General Circulation Model (OGCM) experiments that even when the imposed boundary conditions at the ocean surface are symmetric about the equator, a zonally averaged circulation can arise which is meridionally asymmetric (Bryan 1986; Maier-Reimer & Mikolajewicz 1989; Weaver & Sarachik 1991). These OGCM results buttressed earlier multiple equilibria obtained with box models, which were summarized recently by Welander (1986) and by Thual & McWilliams (1992).

The problem can be illustrated in the following simple idealized form. Let us represent a zonally averaged ocean by a slender rectangular box which is filled with a salt solution, and assume that three sides of the box, say, the sidewalls and the bottom, are insulated and are impermeable to salt. At the top boundary, identical symmetric functions of temperature, T, and salinity, S, are maintained at all times. Following previous workers, we shall call these 'restoring boundary conditions'. The unique steady-state solution of this fluid system consists of two cells which are symmetric about the vertical centreline of the enclosure as shown later. From this steady state one can calculate the salt flux across the top of the enclosure.

Now let us consider a second idealized problem as follows. We shall use the same restoring condition for the temperature as in the first problem, but across the top boundary replace the prescribed salinity with a salt-flux condition, which is calculated from the steady state of the first problem. Theoretically the solution of the first problem is also a solution of the second one. The solution for the salinity equation of the second problem is, however, no longer unique, because all boundary conditions imposed on it are now in flux form, i.e. the salinity equation has Neumann rather than Dirichlet boundary conditions. If we add any constant to the original solution, the result is also a solution.

The usual remedy for this non-uniqueness is to add a compatibility condition. The additive constant in the salinity, however, does not affect the flow fields, which depend on the density gradient – rather than on the density – of the fluid. For the problem studied in this paper, such a compatibility condition need therefore not be applied. For some of the experiments, the average S over the enclosure was subtracted from S at each grid point for every time step. This procedure eliminates the linear trend in S as a function of time, but it does not affect the flow fields and the temperature field.

It turns out that in the second problem with a salt-flux condition, the two-cell solution is unstable to infinitesimal perturbations. The circulation to which the flow stabilizes is asymmetric about the vertical centreline in the sense that one cell becomes larger than the other. In fact, for sufficiently high Rayleigh number, the flux condition transforms the two-cell into a one-cell circulation. Since the asymmetry can take on two forms, i.e. the larger cell can either be on the right or on the left, the transition from symmetric to asymmetric flow arises as a pitchfork bifurcation (Guckenheimer & Holmes 1983; Ghil & Childress 1987). A bifurcation diagram based on our numerical experiments is presented in Appendix C (figure 16). Thus the oceans can acquire quite different steady states if a salt-flux condition is used instead of a restoring condition. The former is a more realistic boundary condition for the oceans, where it corresponds to a given evaporation-minus-precipitation flux.

In the case of the Atlantic Ocean, the zonally averaged meridional circulation is at present a one-cell circulation from pole to pole instead of a two-cell circulation symmetric about the equator. The latter is the expected response to a forcing function symmetric about the equator. The surface flow in the Atlantic is from south to north. At high latitudes there are small sinking regions where the warm salty water transported north from the equator is cooled down by atmospheric conditions, and sinks in the form of deep convection. The cold waters resulting from deep convection make up a return flow southward in the abyssal regions of the Atlantic Ocean. This picture of the general circulation of an ocean is highly simplified. In fact the Pacific Ocean behaves quite differently from the Atlantic, with waters rising in its northern part. The Atlantic and the Pacific oceans interact dynamically through the Antarctic Circumpolar Current and through atmospheric fresh-water fluxes to form a very complex system. Stommel (1961), Rooth (1982), Welander (1986) and others, by using simple box models, and Kagan & Maslova (1990), by using a three-layer model, had arrived at possible multiple equilibria for this system.

These multiple equilibria have attracted a substantial amount of attention recently, being perceived as closely related to the glaciation cycles of the Quaternary era (Broecker, Peteet & Rind 1985; Duplessy & Shackleton 1985; Ghil, Mullhaupt & Pestiaux 1987; Duplessy *et al.* 1988; Shackleton *et al.* 1988) and to interdecadal oscillations of the ocean–atmosphere system (Manabe & Stouffer 1988; Ghil & Vautard 1991). Marotzke, Welander & Willebrand (1988) used a two-dimensional hydrostatic model to illustrate the asymmetric, bifurcated state in a rectangular box. Using oceanic parameters, they studied a problem of very high Rayleigh number. Their conclusions are similar to those found in the OGCM experiments. They have also proposed a positive feedback mechanism to explain the instability which we shall explore later, and concluded that there are no threshold values for multiple equilibria, i.e. as long as a salt-flux boundary condition is applied, one-cell circulation always prevails.

Thual & McWilliams (1992) have extensively studied the bifurcations in a two-dimensional box. They used a non-hydrostatic model and imposed arbitrary salinity-flux conditions, without solving the problem with restoring conditions for the temperature and salinity first as described above. Because of the latter feature, it is hard to determine the correspondence between salinity Rayleigh numbers and thermal Rayleigh numbers in their work, which makes it difficult to directly compare our results with theirs.

In this paper, we investigate a similar problem by solving numerically the two-dimensional Navier–Stokes equations and the full transport equations for heat and salt by a finite-difference method (Quon 1976, 1987). We examine the bifurcation structure as a function of the Rayleigh number Ra and the salt-flux strength γ, and show that there are thresholds for both Ra and γ below which bifurcation does not take place.

In §§2 and 3, we present the model and the numerical methods. In §4 we report the results of our numerical computations. A stability curve based on the results of these numerical experiments is presented in §5. Conclusions and suggestions for future work follow in §6. In Appendices A and B, we construct explicitly approximate two-dimensional symmetric solutions, for low and high Ra, in order to help understand some of our numerical results. The stability curve in §5 is complemented by the bifurcation diagram in Appendix C.

2. The model

The model consists of a rectangular box of arbitrary height-to-length aspect ratio, $d \equiv H/L$, as depicted in figure 1. In the geophysical context, we can consider this model as a crude representation of the zonally averaged latitude–depth cross-section of a world ocean. Arguments for the exclusion of rotation are given by Marotzke *et al.* (1988) and by Thual & McWilliams (1992). We approach this idealized problem

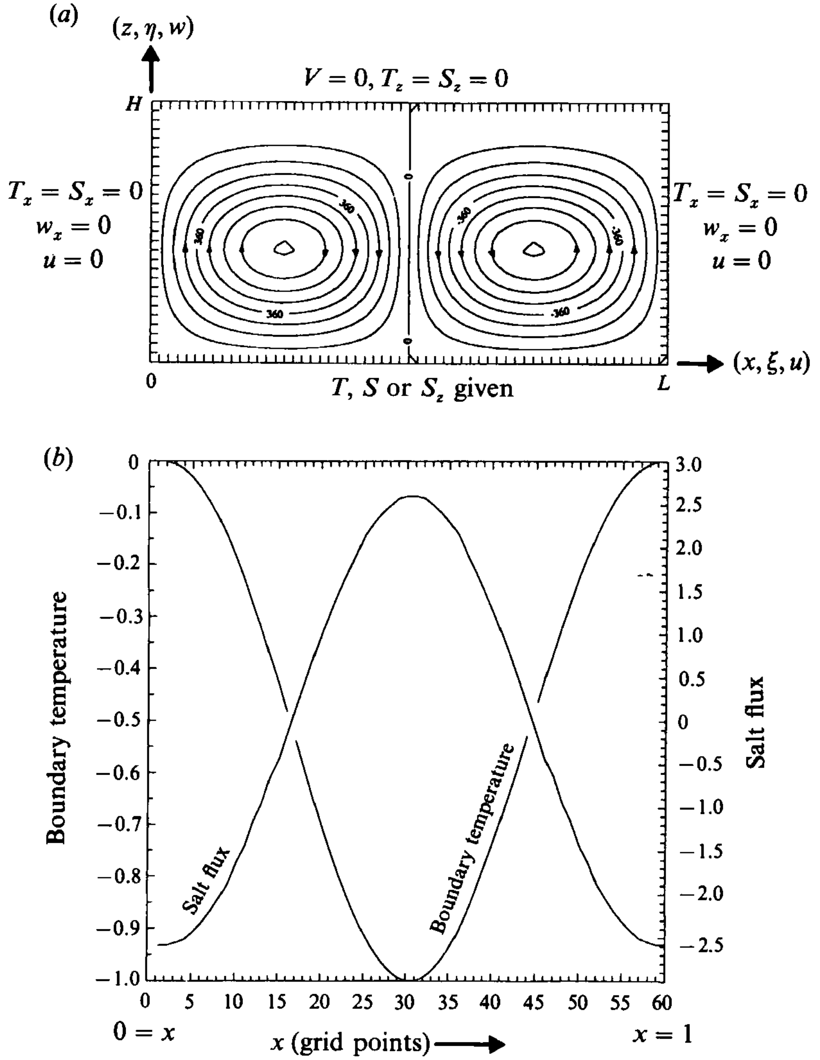

FIGURE 1. (*a*) The physical model with T and S boundary conditions indicated and the expected symmetric solution. Contour interval for the stream function $\psi(x,z)$ is 9×10^{-4} non-dimensional units. (*b*) Temperature (salinity) values imposed at the boundary and a typical salt-flux distribution along it computed from a symmetric steady state.

in an exploratory fashion, covering a wide range of parameters, with the values relevant to planetary-scale flow representing a small subset of this range.

We impose the restoring conditions at the bottom boundary instead of the top for convenience, because we already have a model that was thoroughly calibrated on a different thermal convection problem (Quon 1987). As a result, the fluid will sink near the vertical symmetry axis, rather than rising there, as in previous work with the restoring boundary conditions at the top: the two sets of results are simply a reflection of each other in a horizontal symmetry axis.

We introduce a Cartesian coordinate vector $\boldsymbol{X}=(x,z)$ and a velocity vector $\boldsymbol{V}=(u,w)$, and use the following characteristic values to non-dimensionalize the equations: lengthscale L, L being the length of the box, velocity scale $U=(\kappa_T\,\nu)^{\frac{1}{2}}/L$, κ_T and ν being respectively the thermal diffusivity and kinematic viscosity, timescale

$\tau = L/U$, and temperature and salinity scales ΔT and ΔS, which are respectively the maximum temperature and salinity differences in the enclosure. However, when the salt flux is specified, the maximum difference, ΔS, will be different from that when the restoring condition is specified on the boundary. From our computations, ΔS is of the same order of magnitude for both sets of conditions.

The two-dimensional governing equations are

$$\partial u/\partial t + u\,\partial u/\partial x + w\,\partial u/\partial z = -\partial p/\partial x + \sigma^{\frac{1}{2}}\nabla^2 u, \tag{2.1}$$

$$\partial w/\partial t + u\,\partial w/\partial x + w\,\partial w/\partial z = -\partial p/\partial z + Ra(T-\lambda S) + \sigma^{\frac{1}{2}}\nabla^2 w, \tag{2.2}$$

$$\partial T/\partial t + u\,\partial T/\partial x + w\,\partial T/\partial z = 1/\sigma^{\frac{1}{2}}\nabla^2 T, \tag{2.3}$$

$$\partial S/\partial t + u\,\partial S/\partial x + w\,\partial S/\partial z = \eta/\sigma^{\frac{1}{2}}\nabla^2 S, \tag{2.4}$$

$$\operatorname{div} \boldsymbol{V} = 0, \tag{2.5}$$

with the following boundary conditions:

$$\boldsymbol{V} = 0 \quad \text{at } z = d, \tag{2.6a}$$

$$\partial u/\partial z = w = 0 \quad \text{at } z = 0, \tag{2.6b}$$

$$u = \partial w/\partial x = 0 \quad \text{at } x = 0, 1, \tag{2.6c}$$

$$\partial T/\partial n = \partial S/\partial n = 0 \quad \text{at } z = d, x = 0, 1, \tag{2.6d}$$

where $\partial/\partial n$ denotes the normal gradients on the respective boundaries. A special role will be played by the temperature and salinity boundary conditions:

$$T = T(x) = S(x) = \tfrac{1}{2}(\cos 2\pi x - 1) \quad \text{at } z = 0, \tag{2.6e}$$

or

$$T = T(x), \quad \partial S/\partial z = \gamma f(x) \quad \text{at } z = 0. \tag{2.6f}$$

Here $f(x)$ is the salinity gradient (salt flux) calculated from the symmetric state using boundary condition (2.6*e*), γ being a free parameter to be discussed later. Note that at the sidewalls only free-slip conditions are imposed, in order to make the vertical boundaries of the model similar to the natural conditions in the ocean. Unfortunately, this will also make it more difficult to model the flow in the laboratory. We believe, however, that the free-slip sidewalls do not alter the basic dynamics of the problem. Note that (2.2) shows that T and S have directly opposite effects on the flow, accelerating or decelerating it according to the respective sign of their gradients.

The main non-dimensional parameters are

$$Ra = \alpha g \Delta T L^3/(\kappa_{\mathrm{T}}\nu), \quad \text{the (thermal) Rayleigh number,} \tag{2.7a}$$

$$\lambda = \beta\Delta S/(\alpha\Delta T), \quad \text{the salt-to-heat buoyancy ratio,} \tag{2.7b}$$

$$\eta = \kappa_{\mathrm{S}}/\kappa_{\mathrm{T}}, \quad \text{the Lewis number (the ratio of salt and heat diffusivities),} \tag{2.7c}$$

and

$$\sigma = \nu/\kappa_{\mathrm{T}}, \quad \text{the Prandtl number,} \tag{2.7d}$$

based on the following equation of state

$$\rho = \rho_0(1 - \alpha T\Delta T + \beta S\Delta S); \tag{2.7e}$$

here κ_{S} is the coefficient of diffusivity for the salinity, while α and β are the coefficients of volume expansion for heat and salt, respectively. Now if we include the parameter γ, which is introduced in (2.6*f*) to denote the salt-flux strength (the original salt flux has $\gamma = 1$), we have the following parameter set for the problem:

$$\Omega \equiv (Ra, \gamma, \lambda, \eta, \sigma, d). \tag{2.8}$$

For water, $\sigma = O(10)$, $\lambda = 0.32$, $\eta = O(10^{-2})$. The parameters listed in (2.8) form a complete set, according to Buckingham's Π-theorem (Barenblatt 1979).

The parameter set Ω is obviously too large for any systematic investigation to cover all of it. We shall show later that the essential parameters for bifurcation are the Rayleigh number, Ra, and the salt-flux strength, γ.

3. Numerical and computational aspects

3.1. *Numerical method*

Equations (2.1)–(2.7) have been solved by a finite-difference method using stretched coordinates (Quon 1976) that already helped solve successfully a number of thermal convection problem in rotating and non-rotating frames of reference (Quon 1980, 1983, 1987). We give therefore only an outline of the method here.

The basic idea of the stretching is to resolve the boundary layers near the walls, without an undue increase in computational burden. With the transformation $x \rightarrow \xi(x)$, $z \rightarrow \zeta(z)$, (2.1)–(2.5) become

$$\partial u/\partial t + \boldsymbol{V}\cdot\mathscr{A}u = -(\partial\xi/\partial x)(\partial p/\partial\xi) + \sigma^{\frac{1}{2}}\mathscr{L}u, \tag{3.1}$$

$$\partial w/\partial t + \boldsymbol{V}\cdot\mathscr{A}w = -(\partial\zeta/\partial z)(\partial p/\partial\zeta) + Ra(T-\lambda S) + \sigma^{\frac{1}{2}}\mathscr{L}w, \tag{3.2}$$

$$\partial T/\partial t + \boldsymbol{V}\cdot\mathscr{A}T = 1/\sigma^{\frac{1}{2}}\mathscr{L}T, \tag{3.3}$$

$$\partial S/\partial t + \boldsymbol{V}\cdot\mathscr{A}S = \eta/\sigma^{\frac{1}{2}}\mathscr{L}S, \tag{3.4}$$

$$\mathscr{A}\cdot\boldsymbol{V} = 0, \tag{3.5}$$

where $\mathscr{A} = (\boldsymbol{i}\,\partial\xi/\partial x)(\partial/\partial\xi) + (\boldsymbol{j}\,\partial\zeta/\partial z)(\partial/\partial\zeta)$ and $\mathscr{L} = \mathscr{A}\cdot\mathscr{A}$ are the two-dimensional gradient and Laplace operators in the transformed coordinates, $\boldsymbol{i}$ and $\boldsymbol{j}$ being unit vectors in the x- and z-direction, respectively. A diagnostic equation for the dynamic pressure is obtained by operating on (3.1) with $(\partial\xi/\partial x)(\partial/\partial\xi)$ and on (3.2) with $(\partial\zeta/\partial z)(\partial/\partial\zeta)$, and adding the resulting equations:

$$\mathscr{L}p = -\partial(\mathscr{A}\cdot\boldsymbol{V})/\partial t + \mathscr{Q}(u, w, T, S), \tag{3.6}$$

where $\mathscr{Q}(u, w, T, S)$ represents the rest of the terms in (3.1) and (3.2) after the operation.

Equation (3.6) is elliptic with variable coefficients. The boundary conditions for (3.6) are obtained from (3.1) and (3.2). Since $\mathscr{A}\cdot\boldsymbol{V}$ on the right-hand side of (3.6) does not vanish in finite-difference form because of machine round-off errors, it is retained in the equation, and unknown at future time levels. The best approximation is to assume $\mathscr{A}\cdot\boldsymbol{V}$ in the future to be zero (Quon 1976; see also Chorin 1968, 1969).

The stretched coordinates are based on the following strictly-monotonic transform function:

$$\xi(x) = 0.5(N+1) + 0.5(N-1)\times\frac{\ln[(b+x-0.5)/(b-x+0.5)]}{\ln[(b+0.5)/(b-0.5)]}, \tag{3.6a}$$

$$b^2 = 0.25/(1-2s), \quad 0 \leqslant x \leqslant 1, \tag{3.6b}$$

where s is a stretching parameter and N is the number of grid points in the x-direction. For each value of x, there is a corresponding value for ξ, with $0 \leqslant x$, $\xi \leqslant 1$. The transformation for the vertical coordinate is obtained by replacing (x, ξ) by (z, ζ) in the above equation.

For the studies reported in this paper, the values of s are 0.45 in ξ and 0.04 in ζ, when their respective ranges are $0 \leqslant \xi \leqslant 1$ and $0 \leqslant \zeta \leqslant 0.2$. These values of s yield fairly uniform transformations throughout the whole range of x and z. Highly contracted grids, corresponding to very small values of s (relative to 1.0 and d), have not been used because the flows are reasonably uniform over the whole domain of integration for the range of Rayleigh numbers we are interested in. An argument can be made for much higher grid resolution in the boundary regions for $Ra = O(10^8)$. However, that would require many more grid points to provide reasonable resolution in the regions away from the boundary. This does not seem to be necessary for the problem we are interested in, as shown below. The computational meshes for which detailed results are reported consist of 60×30 grid points for $d = 0.2$, and 60×60 for $d = 1.0$. A number of experiments with different resolutions were carried out and their accuracy compared with that of the reported results. The comparison with higher resolutions shows that the meshes chosen give accurate results for all *Ra*-values studied. Choosing a fixed mesh for all *Ra* provides consistency, as well as computational simplicity.

The discretization of the equations is on an Arakawa C-grid (Arakawa & Lamb 1977; Quon 1976) by second-order, centred differences and the discrete equations are solved by the alternating direction implicit (ADI) method (Varga 1962).

3.2. *Computational procedure*

The computation of quasi-steady states proceeds by forward integration of the flow equations, in three steps. First, a quasi-steady state is established for a given *Ra* with the restoring boundary conditions for both temperature and salinity specified at the bottom. The quasi-steady state of this first stage of the computation is always a symmetric two-cell circulation, with fluid rising near the sidewalls and sinking at the centre. From the steady-state solution of the salinity equation, the salt flux across the bottom boundary is computed and stored.

In the second stage of the computation, we use the same temperature restoring condition, but replace the boundary condition for the salinity with the flux computed from Stage 1. The computations are carried out with either (*a*) the previous symmetric state as initial data, or (*b*) a zero initial condition for all fields. After an arbitrary duration in this Stage 2, a perturbation of $O(0.1\%)$ of the salinity maximum is introduced on the first grid line next to the bottom boundary in either half of the enclosure to start Stage 3 of the computation.

Sometime during Stage 3 of the computation, the symmetric circulation gives way to a major and a minor cell. The time it takes for the major cell to develop depends on many factors, such as the initial data, the Rayleigh number *Ra*, the salt-flux strength γ, and the aspect ratio d. It seems that the system is inherently unstable. Even machine round-off errors are sufficient, over a broad parameter range, to trigger the instability. This assessment agrees with the observations of Weaver & Sarachik (1991), and of Marotzke *et al.* (1988), who introduced perturbations right at the beginning of Stage 2 for most of their computations. However, our broader parameter sweep indicates that when γ is small, or when d is large, we must introduce a perturbation in order to initiate the finite-amplitude instability within reasonable time.

We have discovered that for $Ra > Ra_0$ (Ra_0 being a critical Rayleigh number), when bifurcation is expected, there exists a value of $\gamma < 1$ below which bifurcation is suppressed. On the other hand, when $Ra < Ra_0$, and bifurcation is not expected, there exists a value of $\gamma > 1$ above which bifurcation does appear. For a given *Ra*, the major cells vary in size depending on the value of γ. Similarly, for a given γ, the size of the major cell depends on *Ra*. In the γ-*Ra* space, we can construct a neutral stability curve separating symmetric from asymmetric flows. Next to this curve in the asymmetric regime, the cells are almost equal in size. The asymmetry intensifies as one moves away from the stability curve. We shall discuss this curve in §5 below.

4. Results

As discussed above, temperature and salinity effects tend to counteract each other. There are, therefore, two realizable symmetric states. The flow is either dominated by the salinity field, if $\lambda > 1$, or by the temperature field, if $\lambda < 1$ in (2.2). When the Rayleigh number is sufficiently small, we see in Appendix A that $\psi(x,z,\lambda) = -\psi(x,z,\lambda')$ if $\lambda' = 2-\lambda$, cf. (A 15). The directions of the two flows are opposite to each other, but the functional shapes of the fields are exactly the same. The reason is as follows. If we replace λ by $(2-\lambda)$ in (2.2), the term $Ra(T-\lambda S)$ becomes $Ra(T-2S+\lambda S) = -Ra(T-\lambda S)$ if $T = S$. This holds for the Lewis number $\eta = 1$, which is used for almost all the computations reported in this paper, except where stated otherwise.

For large Rayleigh number, at which the heat and salt transports are dominated by convection, the flow directions of the two symmetric cells are also opposite to each other, as in the case of small Rayleigh numbers. The functional shapes of the fields, however, are no longer similar, because of the boundary-layer flows being different.

We investigate the salinity- and temperature-dominated regimes separately, and concentrate on temperature-dominated flows with $\lambda = 0.32$, the value for water. Only one case study – at high Rayleigh number – in the salinity-dominated regime is presented here, since oceanic flows at present, at least, are in the temperature-dominated regime, with plumes at high latitudes rather than near the equator (see, however, Kennett & Stott 1990, 1991, for possible past ocean circulations with substantial warm saline deep water formed at low latitudes). The low Rayleigh number flows in the former regime can be inferred from those in the latter regime, studied in §4.2. In order to maintain continuity in the discussion of the temperature-dominated regime, we present the salinity-dominated flows first (which might also be the correct geological sequence of events).

Before proceeding with the study of the flows in a two-component fluid, we consider the question whether or not a one-component fluid can lead to an asymmetric circulation. We have performed an experiment with temperature forcing only, at $Ra = 5\times10^6$. After the flow had reached a quasi-steady state, its heat flux was used as the bottom boundary condition. The flow remains symmetric (not shown). Multiplicity of equilibria and symmetry breaking, at least in a two-dimensional situation, seem to be associated only with the two-component fluids that are our main concern here.

4.1. *Salinity-dominated regime*

In this subsection we describe a solution with $\lambda = 2-0.32 = 1.68$, $Ra = 10^8$, $d = 0.20$, which will be compared with the equivalent case in the temperature-dominated regime having $\lambda = 0.32$, as shown in figures 6 and 8 below.

4.1.1. *Symmetric flows*

Figure 2 shows the salinity, S, and the stream function, ψ, of the symmetric flow. In the symmetric regime, when the same restoring boundary condition is applied to both the temperature and salinity equations, the salinity distribution is exactly the same as that of the temperature for $\eta = 1$. Therefore we display only the temperature or the salinity of the symmetric flows.

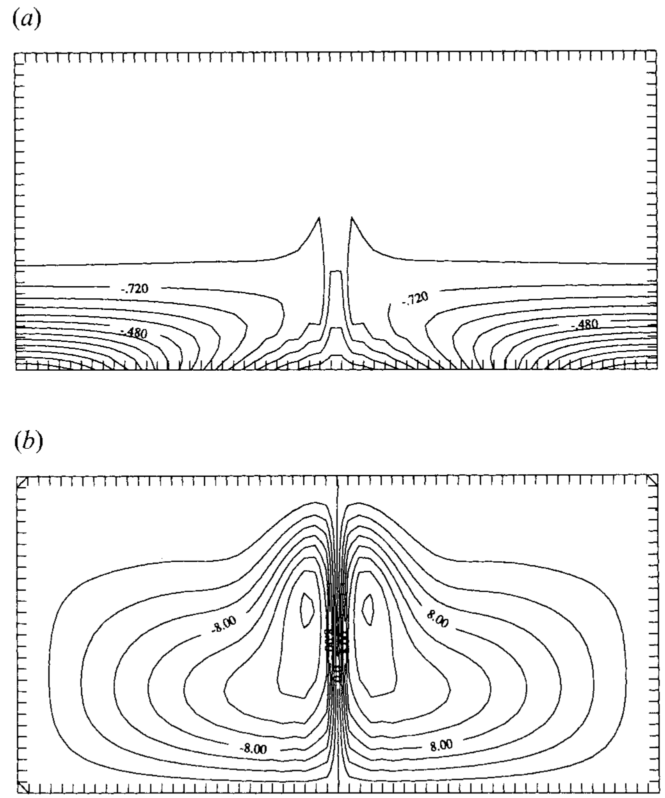

FIGURE 2. The symmetric state of a salinity-dominated flow with $\lambda = 1.68$; restoring boundary conditions for both T and S. (*a*) Salinity (or temperature), and (*b*) the stream function; contour intervals are 0.06 and 2.00 units, respectively. The contour plots for all cases with $d = 0.20$ are exaggerated by a factor of 2.5 in the vertical, for clarity.

The isohalines in figure 2(*a*), and the stream lines in figure 2(*b*), exhibit a plume at the centre of the enclosure. On both sides of the centreline the isohalines slope upward toward the centre (figure 2*a*). Since density is dominated by salinity, the fluid is gravitationally unstable in this area. From this unstable region emanates a very strong internal jet, which forms an internal boundary layer, as shown in figure 2(*b*). The return flows from this internal jet form a pair of anti-symmetric cells. These cells are highly distorted, with their maxima situated back to back next to the centreline of the box. At low Rayleigh number, on the other hand, the cells are symmetric about their respective centrelines at $\frac{1}{4}$ distances from each sidewall, cf. figure 4(*b*) below. In contrast, the temperature-dominated regime has plumes and cell maxima near the sidewalls of the enclosure for high *Ra*.

If we compare the flow fields and the temperature and salinity of this case and those of the corresponding temperature-dominated case shown in figure 6(*b*), we see a nearly one-to-one correspondence; the right-hand cell of one case is the left-hand cell of the other. The side boundaries produce no change of symmetry because the imposed free-slip conditions are also satisfied naturally by the stream function at the centreline when the flows are antisymmetric. The jets are located where the fluid is gravitationally unstable. The mechanism that creates the jet is very similar to that in the one-component problem studied by Daniels & Stewartson (1977, 1978) and by Quon (1987).

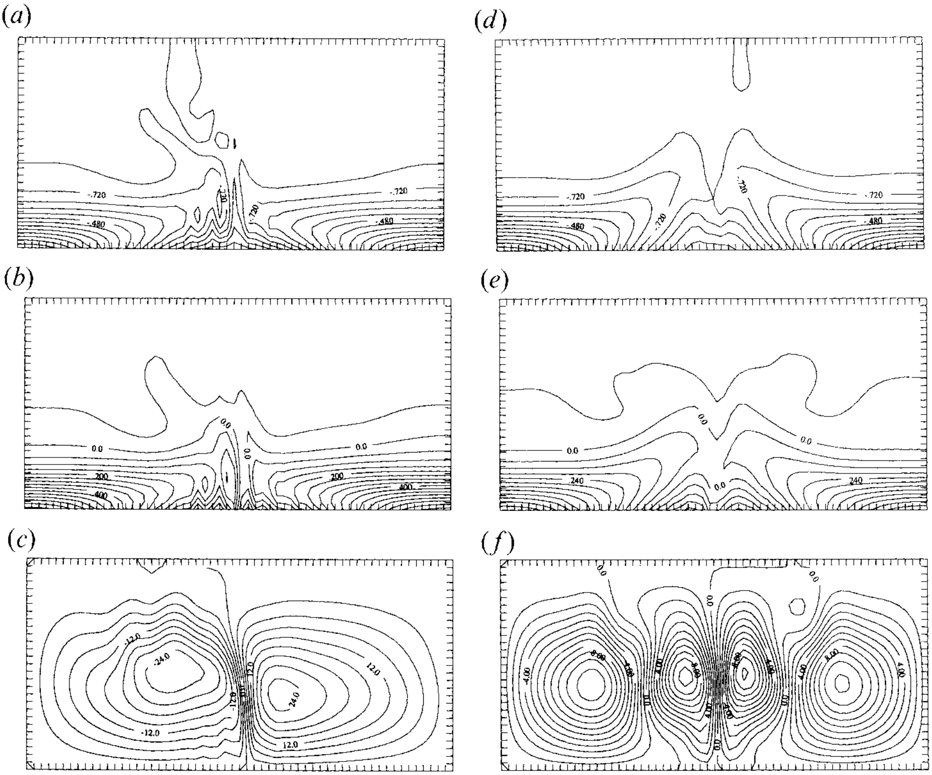

FIGURE 3. An asymmetric state of the salinity-dominated case, $\lambda = 1.68$; salt-flux condition. (*a*) Temperature, (*b*) salinity, and (*c*) stream function at timestep 160 k; (*d*) temperature, (*e*) salinity, and (*f*) stream function at timestep 300 k. Contour intervals are 0.06 for temperature and salinity; they are 3.00 for the stream function in (*c*) and 1.0 in (*f*), respectively.

Transition to a one-cell circulation is tantamount to a symmetry-breaking bifurcation. The salinity- and temperature-dominated regimes after bifurcation no longer display such a simple correspondence between the one and the other as in the symmetric case.

4.1.2. *Asymmetric flows*

Figure 3(*a–f*) shows the asymmetric states of temperature, salinity and stream function at two widely separated timesteps, (*a–c*) at timestep 160 k, and (*d–f*) at timestep 300 k, where 1 k = 1000 steps. After the flux condition has been applied at the bottom boundary, the flow seems to be remarkably stable. The small asymmetries in figures 3(*a*)–3(*c*) develop very slowly, and do not show the explosive growth seen for the temperature-dominated regime (cf. figure 12). The present salinity-dominated case takes more than 110 k timesteps for the cells to show even minute asymmetry. On the other hand, the temperature-dominated case shown in figure 6 takes only 20 k timesteps to reach a noticeably asymmetric state from a symmetric one, and the explosive growth from this slightly asymmetric state to a completely new one-cell circulation takes less than 5000 timesteps. The dimensionless time step, $\delta t = 4 \times 10^{-6}$, is exactly the same in both cases.

At 160 k, wavy motion is apparent in the left-hand cell, while the right-hand cell appears quite smooth (figure 3*c*). Corresponding to this wavy motion, both the temperature and salinity plots exhibit some detached or nearly detached contours (figure 3*a, b*), indicating some fairly vigorous flow. The left-hand cell is not preferred for wavy motions to appear. At other times, it is the right-hand cell that is wavy, while the left-hand cell remains smooth. The two types of motion alternate quasi-periodically between the cells for some time. Subsequently the cells split into four as shown in figure 3(*d–f*), and further into a maximum of six cells (not shown). Although the cells are never completely symmetric about the centreline of the cavity, there is always an equal number of similar cells in each half of the cavity. The circulation reverts to four and two cells again from a configuration of six cells. The computations were not carried out long enough to see many of these reversals. However, at no time does one cell dominate the others – as will occur in the temperature-dominated case (see figure 8) – while the turbulence-like structure of the isotherms and isohalines seen here never appears in the temperature-dominated cases studied below. The circulation for the salinity-dominated flows with a salt flux condition is in fact very similar to Bénard convection.

We have not been able to obtain a quasi-steady state in this case, but symmetry breaking appears to be definitely more difficult here than in the corresponding temperature-dominated case. We can certainly not obtain a one-cell circulation for the former case. It is clear that although the symmetric states are very similar in both the temperature- and salinity-dominated regimes, the asymmetric states are not. The differences may be due to the fact that, in the temperature-dominated case, the unstable layers are widely separated from each other, while in the salinity-dominated case the unstable layers are adjacent to each other forming an internal layer. In the latter case, the strongest circulations are back to back. Close proximity of the rapid flow regions in the interior seems to make it more difficult for one cell to annihilate the other, and hence the system appears to be a great deal more stable than in the temperature-dominated case. One more important difference between the salinity- and temperature-dominated cases is that we have applied the flux condition on the dominant component, S, instead of the dominated component, T (in contradistinction from the temperature-dominated cases studied below, where the flux condition is applied to the dominated component).

It follows that the two regimes behave quite differently in our model if we maintain the functional forms of the boundary conditions for T and S the same, but vary their amplitudes to effect either a temperature- or salinity-dominance. Thual & McWilliams (1992) indicate that their model could yield asymmetric results for the salinity-dominated flows. It is not clear how severe the asymmetry is and where asymmetry can be realized in the salinity–thermal Rayleigh number space. In addition, they used a much smaller aspect ratio, $d = O(0.05)$, instead of the value $d = 0.20$ used here.

4.2. *Temperature-dominated regime*

We concentrate on this regime, since it is more realistic in terms of the ocean circulation for the present and recent geological past: for the last 25 million years or more (Kennett & Stott 1990), deep waters have formed in plumes in polar seas, rather than in the vicinity of the equator.

4.2.1. *Symmetric flows*

When we apply the restoring T and S boundary conditions at the bottom, the quasi-steady states are symmetric about the vertical centreline for both the temperature- and salinity-dominated cases. The circulations consist of two cells, each filling up half of the cavity regardless of the values of the Rayleigh number Ra and aspect ratio d. The T and S distributions, however, show great differences at

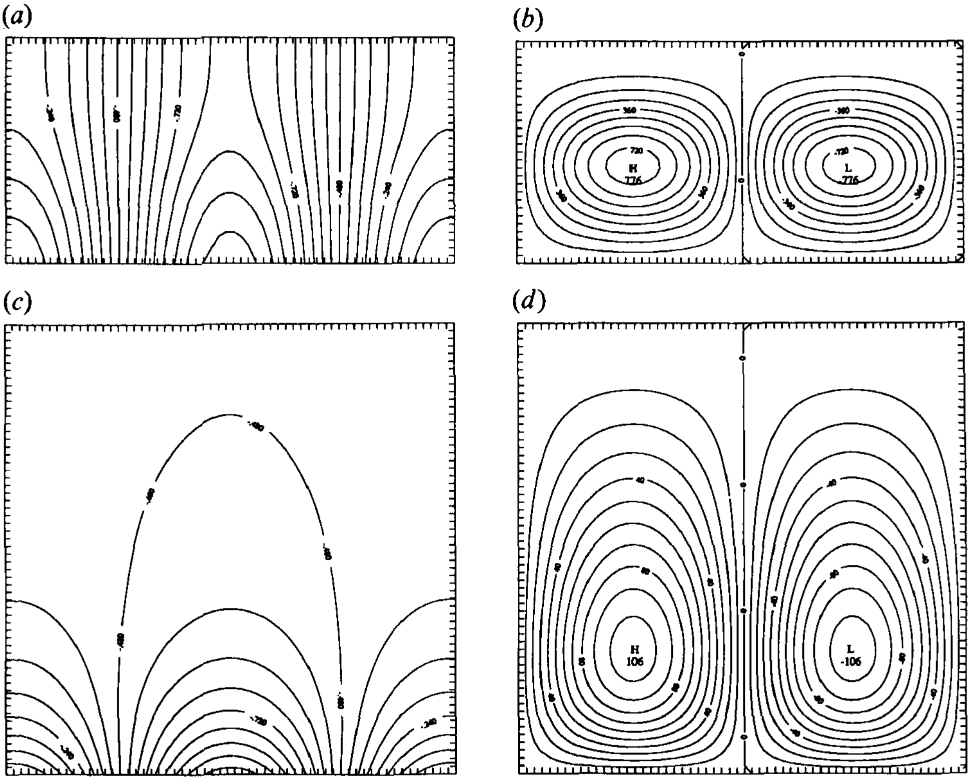

FIGURE 4. Symmetric flows at low $Ra = 10^3$. (*a*) The temperature, and (*b*) the stream function for $d = 0.2$; (*c*) temperature, and (*d*) stream function for $d = 1.0$. Contour intervals are 0.06 for temperature, 9×10^{-5} for ψ in (*b*) and 10^{-2} in (*d*); ψ-values are scaled by the respective multipliers.

different Rayleigh numbers in accordance with their respective boundary-layer thicknesses.

(i) *Low and intermediate Rayleigh number flow*, $Ra = 10^3$ *and* $Ra = 5 \times 10^6$

In this subsection, we investigate the steady symmetric states at $Ra = 10^3$ and $Ra = 5 \times 10^6$ with aspect ratios $d = 0.20$ and 1.0. The former belongs to the low-Rayleigh-number regime. While $Ra = 5 \times 10^6$ would normally be considered to belong to the high-Rayleigh-number regime in thermal convection problems (Quon 1972), we consider it as intermediate here because we shall include much higher Rayleigh numbers, up to $Ra = 2 \times 10^8$.

At low Rayleigh number, $Ra = 10^3$, the T and S transports are dominated by conduction. Consequently the isotherms and isohalines diffuse over the whole cavity (figure 4*a*) at low aspect ratio. The vorticity fields are solutions of the Poisson equation (A 2) with the horizontal gradients of T and S as the source of diffusion. The streamlines are almost evenly distributed, with no distinct boundary layers (figure 4*b*). When the aspect ratio increases from 0.20 to 1.0, the former being used for most of the computations discussed here, the solutions remain qualitatively very similar. Figures 4(*c*) and 4(*d*) show T and ψ for aspect ratio unity. Note that $T \rightarrow -\frac{1}{2}$ at $z = 1$ (figure 4*c*), which is also predicted by (A 7). If we compare the magnitudes of the stream functions in figures 4(*b*) and 4(*d*), they are 10 times larger in the latter. This is predicted by (A 16) because of the difference in the aspect ratios of the two cases. In fact, these solutions at low Rayleigh number are well approximated by the corresponding analytical solutions given in Appendix A.

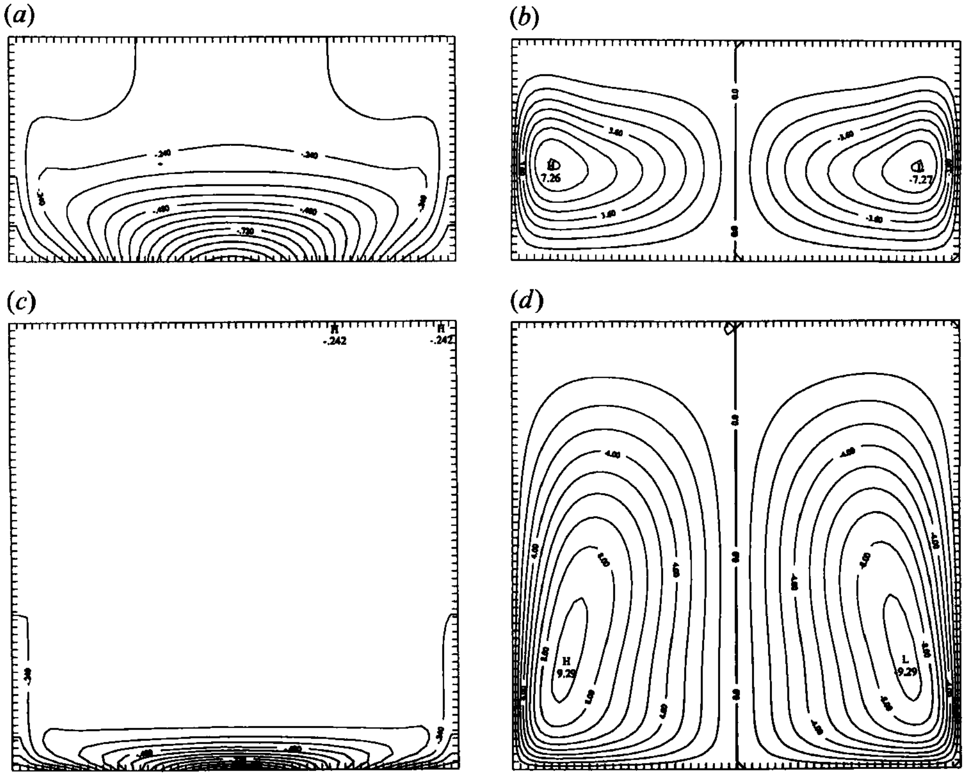

FIGURE 5. Symmetric flows at intermediate $Ra = 5\times10^6$. (*a*) The temperature, (*b*) the stream function for $d = 0.2$; (*c*) temperature, and (*d*) stream function for $d = 1.0$. Contour intervals are 0.06 for temperature and 0.90 for ψ in (*b*) and 1.0 in (*d*).

At intermediate Rayleigh number, $Ra = 5\times10^6$, the boundary layers along the bottom and the side boundaries have become more distinct, as shown in figure 5. Along the top boundary, the flow is very weak. By comparing figures 4 and 5, the differences between low- and intermediate-Rayleigh-number flows are most obvious in the distribution of isotherms (and isohalines). Figures 5(*a*) and 5(*c*) show that the isotherms are more concentrated near the bottom of the cavity for both $d = 0.2$ and 1.0. In spite of the smaller area most of the isotherms occupy, the streamlines still fill the whole interior of the fluid, as in the flows at low Rayleigh number. This is a particularly striking feature when we compare figure 5(*d*) to 5(*c*) for $d = 1.0$. Note that, in the interior, the streamlines are almost vertical and the stream function can be well approximated as a linear function of x.

Of course the flows for intermediate Rayleigh numbers are no longer well represented by the analytical solution for low Ra in Appendix A. One is tempted to invoke the arguments presented in Appendix B for high Ra to explain the interior flows for this particular case. At sufficiently high Rayleigh number, the interior stream function assumes the functional form $\psi(x,z_0) = T_{zz}/T_z(x-\frac{1}{2})$. Hence $\psi = -a(x-\frac{1}{2}) = \psi(x)$ if $T = A\,\mathrm{e}^{-az}$. Furthermore, $\psi = 0$ if T is linear in z. It is interesting that the larger the decay constant a, the larger ψ, provided $T(z)$ is truly exponential. This is no paradox here because the isotherms are compressed by a larger downward velocity when a is large. Unlike the situation at low Rayleigh numbers when the interior flows are generated by thermal forcing in the interior, at high Ra they are forced in the boundary layers. Therefore, in order to understand the

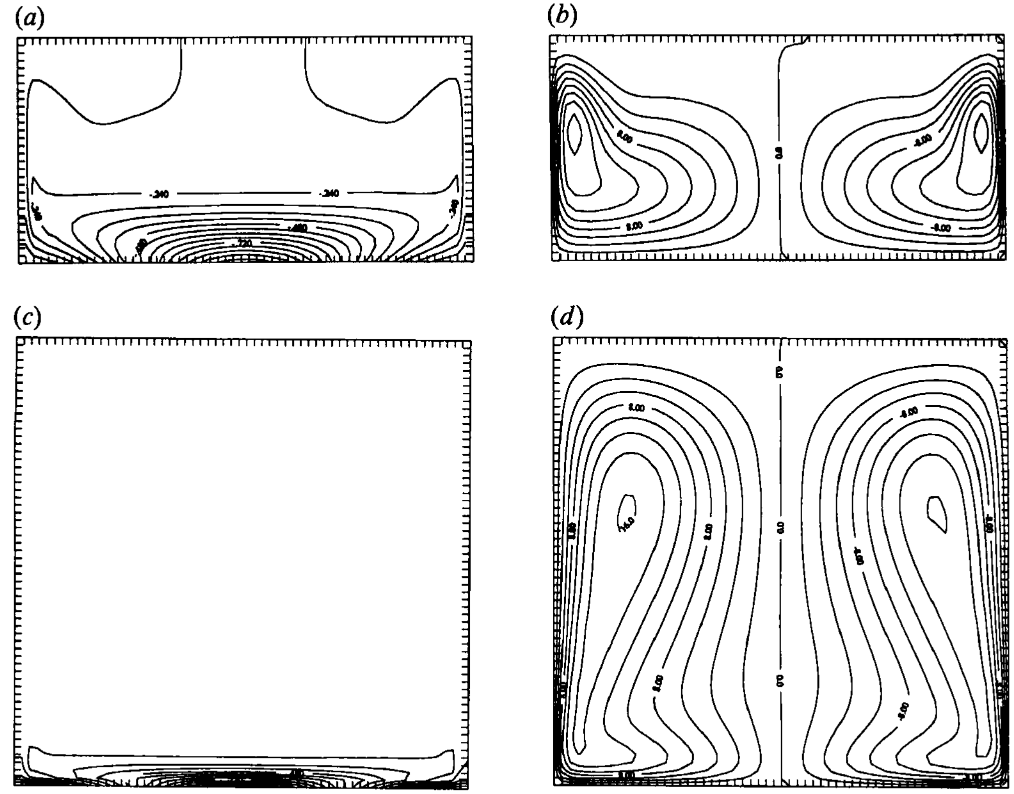

FIGURE 6. Symmetric flows at high $Ra = 10^8$. (*a*) The temperature, and (*b*) the stream function for $d = 0.2$; (*c*) temperature, and (*d*) stream function for $d = 1.0$. Contour intervals are 0.06 for temperature and 2.00 for ψ.

dynamics of the heat and salt transport in the high-*Ra* regime, we must properly resolve the boundary-layer problem. If T is linear, it is most likely governed by diffusion. This implies that the interior velocity is small or zero, and is not important in the heat transport process. We shall examine the interior temperature distribution closely in the next subsection.

(ii) *High Rayleigh number flow*, $Ra = 10^8$

Boundary-layer flows are much more pronounced for $Ra = 10^8$ than those for the lower Rayleigh numbers. There are boundary layers next to the vertical sidewalls and above the bottom, although there is no visible boundary layer below the top boundary. As in the salinity-dominated case, the vertical plumes, or vertical boundary layers, start from areas where the fluid is gravitationally unstable, as shown in figure 6(*a*, *b*); for the present case these regions are near the vertical boundaries. Strong advection in the sidewall boundary layers carries T and S filaments along these walls away from the bottom. Weaker, more diffuse advection due to the return flows in the interior of the cavity compresses the isotherms and isohalines, and confines them to the bottom. Consequently, at high Rayleigh number the isolines of both T and S adhere to the bottom, forming the bottom boundary layer. This is true at both $d = 0.20$ (figure 6*a*) and $d = 1.0$ (figure 6*c*). At $d = 0.20$, there is no real interior, as the entire circulation is within the boundary layer. In comparison with the flows at intermediate Rayleigh number (figure 5*b*), the streamlines extend to a greater height in the sidewall boundary layers. Note especially that the cells are almost identical to those in the salinity-dominated case shown in figure 2(*b*), except that the left- and right-hand cells have interchanged positions, as discussed in §4.1.1.

At $d = 1.0$, the stream function contours for $Ra = 10^8$ are very different from those shown in figure 5*d* for $Ra = 5\times 10^6$. The most significant contrast between the two flow patterns is that, at $Ra = 10^8$, the streamlines in the interior are not vertical straight lines, indicating nonlinear effects. They are, however, still evenly spaced in the horizontal, and can be well approximated by a linear function of x, as they were for $Ra = 5\times 10^6$. The dynamics of the system at both Rayleigh numbers are very much controlled by the boundary layers, although at the higher Rayleigh number advection of momentum in the interior has become important. Hence the infinite Prandtl number argument presented in Appendix B is no longer valid. Note that in figure 6(*d*) the stream function maximum is almost twice that shown in figure 5(*d*) (16 *vs.* 9.3). The flows in general, and the boundary-layer flows in particular are much stronger for $Ra = 10^8$.

The boundary-layer thicknesses are inversely proportional to the Rayleigh number raised to an appropriate fractional power (see figures 5(*c*) and 6(*c*) and the quantitative estimate below). Figure 6(*c*) shows that the isotherms (and hence isohalines) are confined to the bottom boundary region as in figure 5(*c*). The absence of isotherm plumes next to the two side boundaries may indicate that the grid spacing is perhaps not fine enough to completely resolve the boundary-layer structure for this particular computation. The qualitative structure of the flows seems to be reasonably well defined.

Since the interior temperature (and salinity) is constant, the flow adjustment is through viscous diffusion wherever advection of momentum is negligible (see Appendix B). The time required by the flows to reach equilibrium in the interior is extremely long. Both cases for $d = 1$ have been run for an even longer time than the others to ensure their steadiness.

In figures 7(*a*) and 7(*b*) the temperature is plotted as a function of z for $Ra = 5\times 10^6$ and for $Ra = 10^8$: at the centre of the container (panel a) and near the sidewall (panel b). For both Rayleigh numbers, the interior temperature is almost constant; near the centre (figure 7*a*) it is in fact of the form $T(z) = T_0-(T_0+1)\,\mathrm{e}^{-az}$, with $T_0 = -0.24$ for $Ra = 5\times 10^6$ and $T_0 = -0.27$ for $Ra = 10^8$. Near the sidewalls (figure 7*b*) the z-dependence of temperature is not monotone, and hence not exponential (see also figures 5(*a*) and 6(*a*)), but it still asymptotes to a (different) constant as the interior is reached.

The temperature inversion near the bottom for both Ra-values (figure 7*b*) is associated with gravitational instability and vigorous motion (figure 7*c*). If we take the vertical positions of the peaks of the inversions as a measure of the bottom boundary-layer thicknesses, the ratio of the two is given by $\frac{4}{2} = \frac{5}{2.5}$ which is very close to $(10^8/5\times 10^6)^{\frac{1}{5}} = \frac{5}{2.77}$.

In figure 7(*c*) horizontal velocity u appears as a function of z, at $x = 0.25$, starting from the bottom boundary, and in figure 7(*d*) vertical velocity w as a function of x, at $z = 0.25$, starting from the left-hand sidewall. If we scale the vertical distance from $z = 0$ in the horizontal bottom boundary layer as $\mu = z/Ra^{-\frac{1}{5}}$ and the horizontal distance from $x = 0$ in the vertical boundary layer as $\nu = x/Ra^{-\frac{1}{4}}$, we find that the maxima of u are at $\mu = 3.91$ and 3.63 (figure 7*c*), and the zero crossings of w at $\nu = 7.93$ and 5.01 (figure 7*d*), for the two Ra-values, respectively. The fact that the u-maxima in the bottom boundary layer are so close to each other in the μ-coordinate indicates

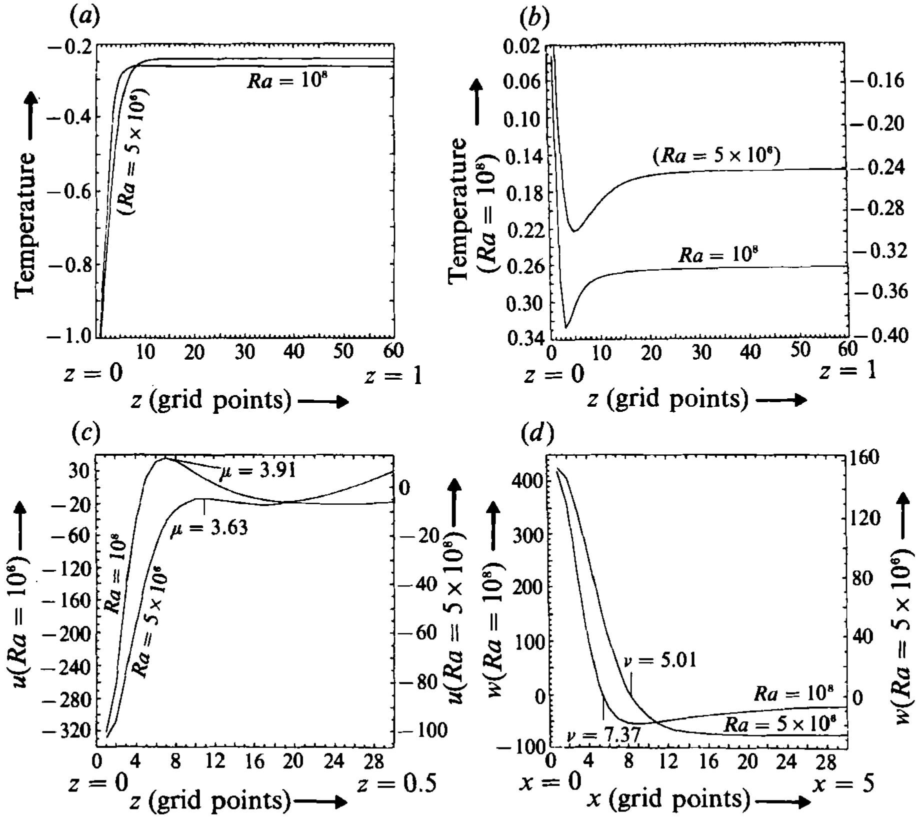

FIGURE 7. Temperature and velocity profiles at $d = 1.0$, for $Ra = 5\times10^6$ and $Ra = 10^8$. (a) Temperature as a function of z at the centre of the container $x = \frac{1}{2}(=\frac{1}{2}L$ in figure 1a); (b) temperature as a function of z at $x = 0.06$ (the 5th grid point from the left-hand wall); note the two different temperature scales for the two different Ra-values in panel (b). (c) Horizontal velocity u as a function of z in the bottom boundary layer at $x = 0.25$; (d) vertical velocity, w, as a function of x in the vertical boundary layer at $z = 0.25$; note the different velocity scales for different Ra in both panels (c) and (d).

that the scaling argument presented in Appendix B describes the bottom boundary layer rather well, and that the grid resolution is also adequate in this region. However, the zero crossings of the vertical velocities in the vertical boundary layer should be closer together. This implies that the higher Rayleigh number computation may benefit from more grid points in the proximity of the vertical boundaries.

To conclude the discussion of symmetric flows, we must point out that when restoring boundary conditions for both T and S are applied, the symmetric circulations are stable even for extremely long computations. The accumulated truncation errors may degrade the accuracy, but do not alter the symmetry. We can argue therefore on firm grounds that the asymmetric flows due to salt-flux conditions discussed below must be physical, and not numerical, phenomena.

4.2.2. *Asymmetric flows*

Contrary to the results of most of the previous investigators, which were more narrowly guided by the oceanographic application and consequently had very high Rayleigh numbers and low aspect ratios, we have found that transition from symmetric to asymmetric states is not inevitable. When it happens, the asymmetry

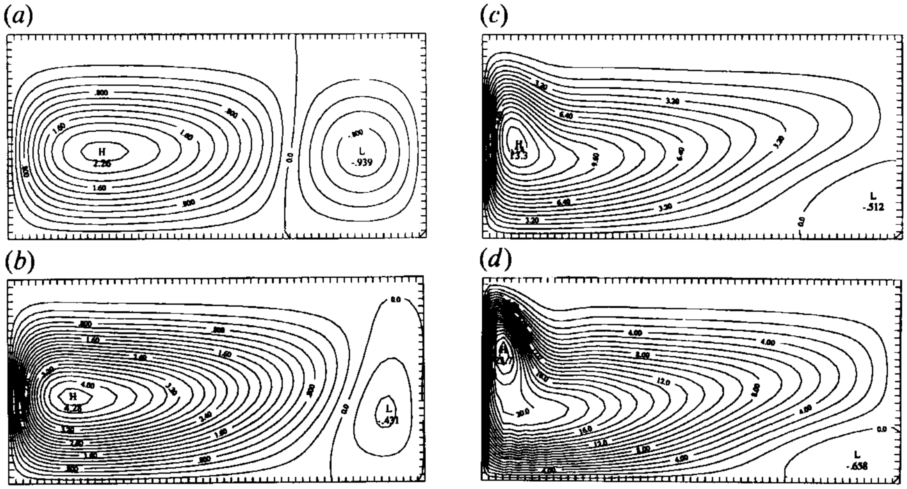

FIGURE 8. Stream function fields for asymmetric states. From (*a*) to (*d*) the Rayleigh numbers are 4×10^5, 10^6, 10^7, 10^8; note how the dominant cell increases with *Ra*. Contour intervals are 0.20, 0.20, 0.80 and 1.00 from (*a*) to (*d*) respectively.

can range from very slight, i.e. the cells being slightly different in size, to catastrophic; in the latter case, one cell completely annihilates the other. There are two separate routes to symmetry breaking. (*a*) It can be reached by varying the Rayleigh number; for all other parameters in Ω fixed, there exists a critical Rayleigh number at which bifurcation occurs, Ra_0. (*b*) With the Rayleigh number and all other parameters in Ω fixed, bifurcation can be attained by varying the salt-flux strength γ. When γ is equal to unity, the problem is the traditional one that encompasses all previous works cited above.

We have found that for a given Rayleigh number, $Ra > Ra_0$, there exists a critical $\gamma < 1$ below which the symmetric flow is stable. On the other hand, for a given Rayleigh number $Ra < Ra_0$, there exists a critical $\gamma > 1$ at which bifurcation will occur. In other words, for a large range of *Ra* encompassing a few decades, bifurcation always occurs. We have not been able to determine, because of computational difficulties, extreme values for *Ra* or γ beyond which bifurcation with respect to the other parameter is completely inhibited. We now examine the asymmetric flows as a function of Rayleigh number at fixed γ, as well as a function of salt-flux strength at fixed *Ra*.

(i) *Rayleigh number variation*, $\gamma = 1$

Once we have realized that the system switches symmetry for a certain Rayleigh number, it is natural to ask whether there is a threshold value for *Ra* below which the symmetric flow is stable for mixed boundary conditions. Equally interesting is the question whether or not the flows will reach the same final, one-cell state for all Rayleigh numbers for which asymmetric flows are possible. We have fixed $\gamma = 1$ as a starting point because that is the situation investigated previously by other authors.

For $\gamma = 1.0$ and $d = 0.2$, the critical Rayleigh number is slightly above 3×10^5. Below that, symmetric flows persist for combined restoring and flux conditions. In figure 8, we show the asymmetric quasi-steady states reached when the salt-flux condition is applied. The range of Rayleigh numbers is 3 orders of magnitude, from 4×10^5 to 1×10^8. Note that for all these diagrams, the perturbations applied in Stage

2 of the computation (see §3.2) are on the left, where the dominant cell is located. Applying the perturbation in the right-hand half of the cavity stimulates the growth of the opposite cell (see figure 13).

As the Rayleigh number increases from 4×10^5 to 1×10^8, the dominant cell grows with it. As the minor cell occupies a correspondingly smaller and smaller portion of the cavity, it also shrinks at the top. This is particularly evident for $Ra = 10^6$, where the minor cell is nearly triangular. At $Ra = 10^7$ and 10^8, the minor cell is almost completely annihilated. The remnants of the minor cell occupy the lower right-hand corner, indicating that the tongue-like intrusion of the major cell is stronger at the top edge. It follows from this figure that the asymmetric states are not always one-cell circulations, while Marotzke *et al.*'s (1988) results and other experiments with OGCMs showed only an extreme, one-cell state.

The asymmetric states change gradually from a two-cell circulation at Rayleigh number 4×10^5 to a one-cell circulation at 10^8. Note also that, as the Rayleigh number increases, the sidewall boundary-layer thickness decreases approximately as $Ra^{-\frac{1}{4}}$ (see Appendix B and figure 7*d*). Since the transition from a symmetric to an asymmetric state is very gradual, it is difficult to determine the critical Rayleigh number, Ra_0, accurately through numerical computation. At $Ra = 3\times10^5$, symmetric cells are quite stable, while at 4×10^5, asymmetric flows set in very fast after the perturbation is added.

(ii) *Variation of the salt-flux strength*, $Ra = 5\times10^6$

Keeping the Rayleigh number constant, one can vary the strength of the salt-flux γ on the boundary, or the buoyancy ratio λ, to achieve bifurcation. Indeed, using $\partial S/\partial z = \gamma f(x)$ is practically the same as changing S to γS in equation (2.2), while the other boundary conditions for S are homogeneous. We have done experiments (not shown) to confirm this qualitative equivalence. Computationally, it is more convenient to vary γ than λ: when using γ, we only need to compute one salt flux for each Rayleigh number, and can perturb the same symmetric state for all γ. Of course, this procedure tacitly assumes that the final state does not depend on the initial one. We have done experiments to confirm this, including the use of a drastically different initial state, that of zero fields. The end results are identical, except that it takes a somewhat shorter time to reach the final asymmetric state when the non-zero symmetric state is used as initial data. We can also consider γ as a free parameter with no need to relate it to λ; this is in fact what Thual & McWilliams (1992) have done in their study.

Figure 9 shows the quasi-steady asymmetric circulation for $Ra = 5\times10^6$ and three values of γ: 0.40, 0.50 and 0.55. The bifurcation point is near $\gamma = 0.40$. Note that the asymmetry increases with γ. The variations are in fact very similar to those that we have seen in figures 8(*a*)–8(*d*), for different Rayleigh numbers when γ is fixed. Therefore we conclude that each bifurcation point in the γ-Ra space can be reached by varying Ra, γ, or both. In fact we can define a neutral stability curve by using the results of a number of numerical experiments. We discuss this stability curve in §5, after we have studied other relevant parametric variations in the remainder of this section.

(iii) *Effects of unit aspect ratio*, $Ra = 5\times10^6$

It is well known that, as the aspect ratio of the container of a fluid system increases, non-hydrostatic effects become more prominent, and the vertical advection becomes more important. In the case of thermal convection in a rotating fluid which

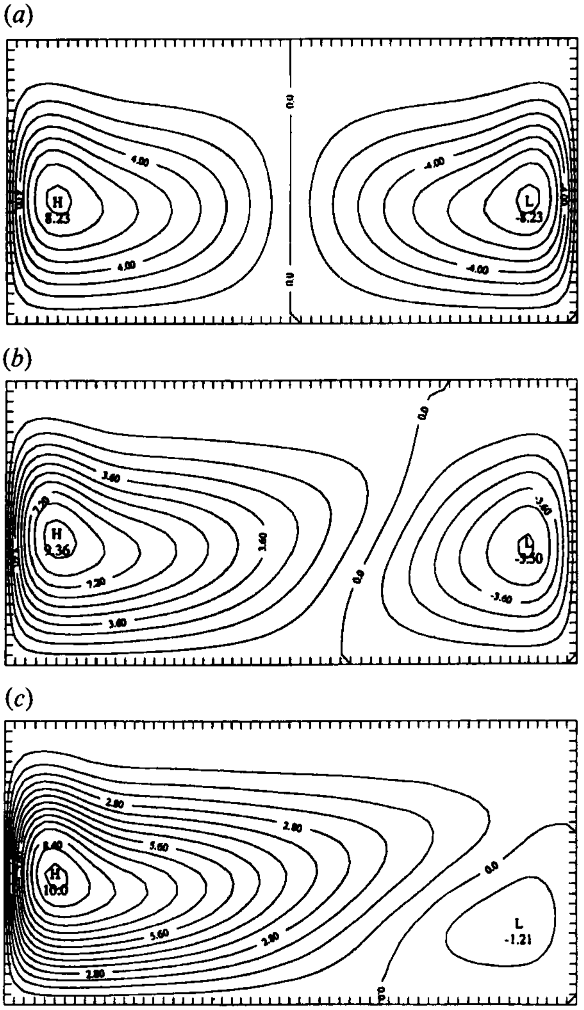

FIGURE 9. Asymmetric stream function fields for $Ra = 5\times10^6$ and increasing γ-values: (*a*) $\gamma = 0.40$, (*b*) $\gamma = 0.50$, and (*c*) $\gamma = 0.55$; note how the dominant cell increases with γ. Contour intervals are 1.00, 0.90 and 0.70 from (*a*) to (*c*) respectively.

is differentially heated from below, aspect ratio $O(1)$ permits many transient vertical modes (Quon 1987); we have also found them in our system. Without entering into a detailed study of the effect of aspect ratio on the generation of asymmetric flows in the present problem, we simply show that bifurcation from symmetric to asymmetric flows is not limited to small aspect ratios, as presented in earlier studies. Specifically we consider flows in a container of aspect ratio equal to unity at $Ra = 5\times10^6$. The temperature (or salinity) and stream function of the symmetric flow for this case were shown in figures 5(*c*) and 5(*d*), and discussed in §4.2.1 (i).

Figure 10 shows T, S, and ψ for the corresponding asymmetric state. The temperature and salinity contours (figure 10*a*, *b*) show typical effects of asymmetric advection. Unlike the symmetric states whose temperature and salinity contours are identical, the T (panel a) and S (panel b) distribution of the asymmetric states are different because of their different boundary conditions. On the other hand, they are very similar to those for lower aspect ratios at comparable Rayleigh numbers.

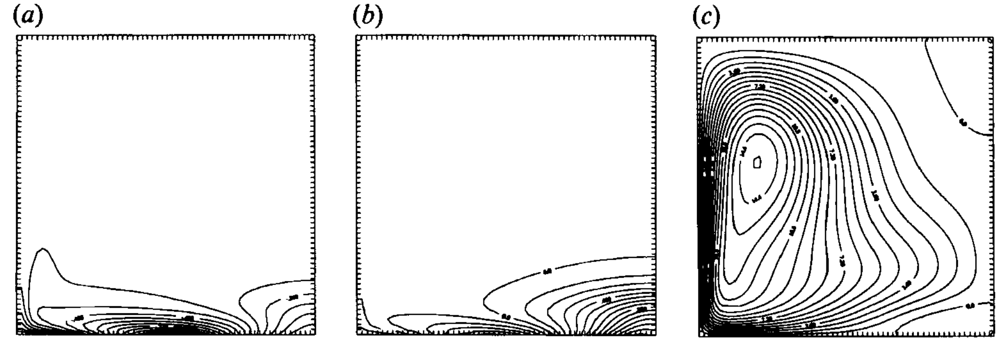

FIGURE 10. The asymmetric state for $d = 1.0$ and $Ra = 5\times10^6$. (a) Temperature, (b) salinity, and (c) stream function. Contour intervals are 0.06 for temperature, 0.10 for salinity and 0.90 for ψ respectively.

It is interesting to compare figure 10(c) with figure 5(d). It is obvious that for aspect ratio $d = 1$, the asymmetric cell has the same vertical scale as its symmetric counterparts. The single cell fills the whole cavity (figure 10c) as it does for $d = 0.2$, despite the fact that the temperature and salinity contours are confined to the bottom boundary layer (figures 10a, b). The interior T- and S-gradients are indeed close to zero and provide therefore no interior forcing. As pointed out in Appendix B, at high Rayleigh numbers the interior flows are not generated locally, but are forced by boundary-layer entrainment or detrainment.

(iv) *Effects of diffusivity ratio, η, and Prandtl number, σ*

For water, the Prandtl number is $\sigma = 7.1$, while $\sigma = 2.25$ was used in our computations so far. While large variations in σ for purely thermal convection can lead to very substantial changes in the route to turbulence (Krishnamurti 1973; Busse 1978), the first one or two bifurcations may be rather insensitive to small changes in Prandtl number. Gill (1966) had even suggested that $\sigma = 7.1$ can be considered as infinite for thermal convection in an enclosure differentially heated on the sidewalls. Our experiments (not shown) confirm that there is little difference between Prandtl number 7.1 and 2.25 in thermosolutal convection. Thual & McWilliams (1992) deleted the advection terms in the vorticity equation entirely, which is equivalent to setting $\sigma \rightarrow \infty$ explicitly (see Appendix B.1 here). We have used a smaller σ mainly for computational convenience.

The correct diffusivity ratio for salt and heat, η, is equal to 10^{-2}, i.e. heat diffuses 100 times faster than salt. For phenomena which crucially depend on the difference in diffusivity, for example the so-called doubly-diffusive problem of salt fingering (Turner 1973), it is important to use the correct ratio. Setting $\eta = 1$, on the other hand, eliminates certain computational difficulties associated with very small diffusivity, such as having to use extremely small timesteps. A mismatch in diffusivities of different components also delays the equilibration process unnecessarily when one is interested only in steady states. The crux of the argument for using a different Prandtl number and a different diffusivity ratio than those of water is that they are of secondary importance in the phenomena we are interested in. In spite of the different values chosen for these parameters in different computations, bifurcation from symmetric to asymmetric flows does occur. It is interesting, however, to see how a reduction in η affects the results, especially the asymmetric state.

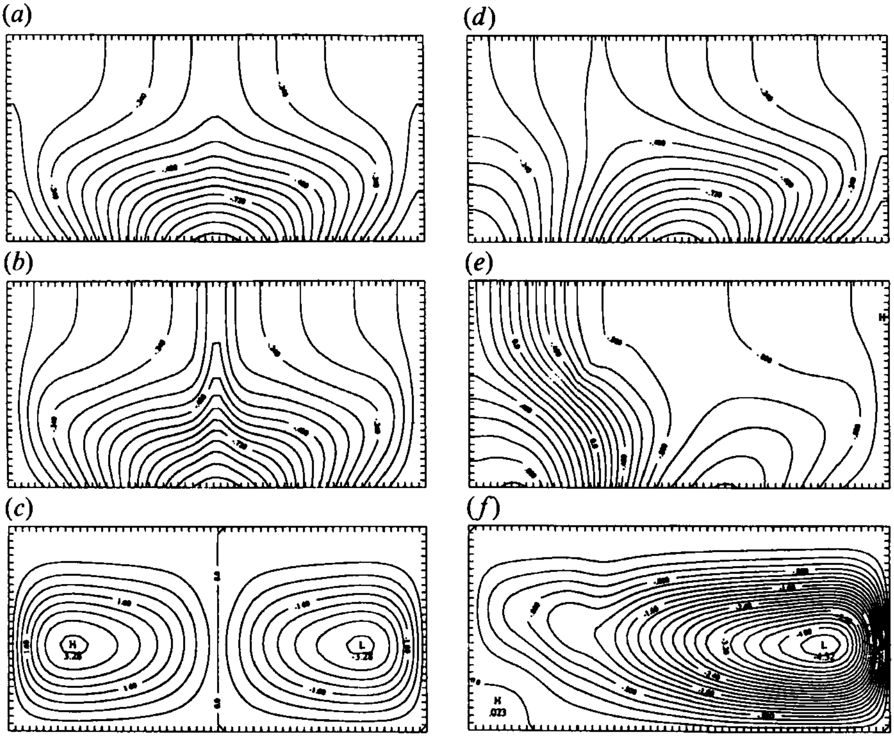

FIGURE 11. The symmetric and asymmetric states of the case with Lewis number $\eta = 0.1$ and $Ra = 10^6$. (*a*) Temperature, (*b*) salinity, and (*c*) the stream function of the symmetric state. (*d*) Temperature, (*e*) salinity, and (*f*) the stream function of the asymmetric state. Note the differences between the temperature and salinity distributions, in both the symmetric and asymmetric case. Contour intervals are 0.06 for temperature and salinity in (*b*), 0.10 for salinity in (*e*), 0.40 for ψ in (*c*) and 0.20 in (*f*).

In this subsection, we discuss the results of a computation for $\eta = 0.10$, i.e. the salt diffusivity has been reduced by an order of magnitude from that in the computations discussed above. Yet η is still an order of magnitude larger than the real value. Figure 11 (*a–c*) shows the symmetric and figure 11 (*d–f*) the asymmetric state of T, S, and ψ at $Ra = 10^6$. The most conspicuous differences between this and the other cases studied in previous subsections appear in the solution of the salt equation. Of course, if $\eta = 1$, the mathematical solutions for both the temperature and the salinity are exactly the same.

In the present symmetric state, however, the isohalines are very much more squeezed in the middle when compared with the temperature distribution. In the asymmetric state, the isohalines are packed more densely on the left-hand side of the cavity than the isotherms, reflecting the less effective diffusive process. The asymmetric stream function seems to have been influenced by this anomaly. The outer streamlines at the left-hand side of the cell, near the bottom, recurve upward, following the salinity contours. This flow pattern resembles better figure 8 (*d*), for $Ra = 10^8$, than figure 8 (*b*), for $Ra = 10^6$, at $\eta = 1$; it is also slightly more realistic than the latter when compared with present-day isopycnals in the Atlantic Ocean (Fuglister 1960; Defant 1961). Thus the effect of Lewis number is qualitatively secondary – bifurcation from symmetric to asymmetric flows still occurs – but quantitatively significant for the resulting asymmetric flow patterns.

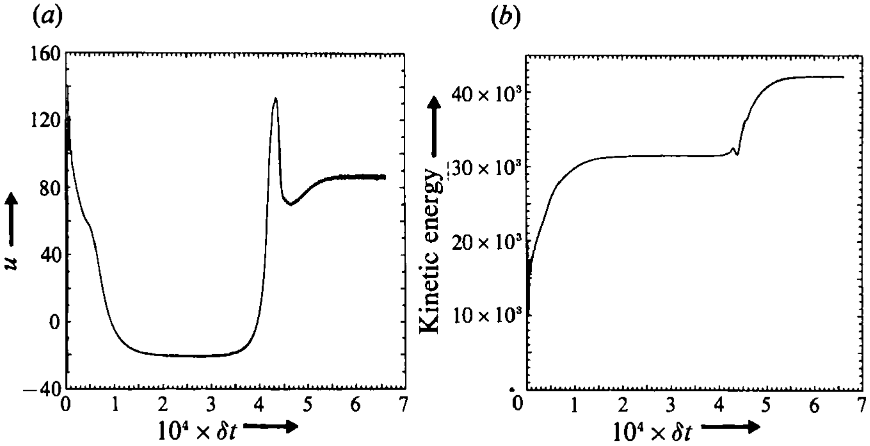

FIGURE 12. Time evolution of the flow for $Ra = 10^8$, $d = 0.2$: (*a*) u-velocity at one point near the lower left-hand corner of the cavity, and (*b*) the integrated kinetic energy. The perturbation is applied at timestep 27 k. The abscissa is in 10^4 timesteps.

4.2.3. *Time evolution near a bifurcation*

It is interesting to follow the transition from a symmetric to an asymmetric state in time, especially through the growth period. Explosive exponential growth marks most of the instabilities that we have described so far. Let us consider the case with $Ra = 10^8$ and $\gamma = 1.0$.

Figure 12(*a*) shows the u-velocity at a point near the lower left-hand corner, and figure 12(*b*) the integrated kinetic energy as a function of time. After the initial growth, the system attains a state of quasi-equilibrium. Even after the switch from restoring to flux condition in S at timestep 23 k, and after the perturbation at timestep 27 k the kinetic energy maintains its equilibrium value for a long time (till about timestep 37 k) before the exponential growth sets in. The growth period is about 4000 timesteps. This case shows an overshoot in the velocity (figure 12*a*). The corresponding integrated kinetic energy also shows a very definite disturbance at the same time, although it is smaller in amplitude.

Figure 13(*a–h*) shows a selected number of contour plots of the stream function and salinity over the growth period. They correspond to 36, 39, 42, and 54 k timesteps, which cover the exponential growth period as shown in figure 12. At 54 k timesteps the one-cell circulation has almost reached its equilibrium. These successive snapshots give a clear image of how the right-hand cell gains strength over the left-hand cell and eventually annihilates it. The time at which the u-velocity attains its maximum at the overshoot corresponds to the time when the left-hand side cell is squeezed into the smallest area (figure 13*c*), before it finally collapses and gets annihilated. For lower Rayleigh numbers the growth process is smooth, and in general there is no overshoot. The process illustrated in figure 13 is fairly representative of the higher-Rayleigh-number bifurcation, but it is not universal.

Note that this case has the exact same parameters as in figure 8(*d*). The cell centre (figure 13*d*) is on the right-hand side because the perturbation was introduced intentionally in the opposite side of the cavity, to show that the dominant cell can grow on either side. It should also be pointed out that figure 13(*d*) has not yet reached equilibrium.

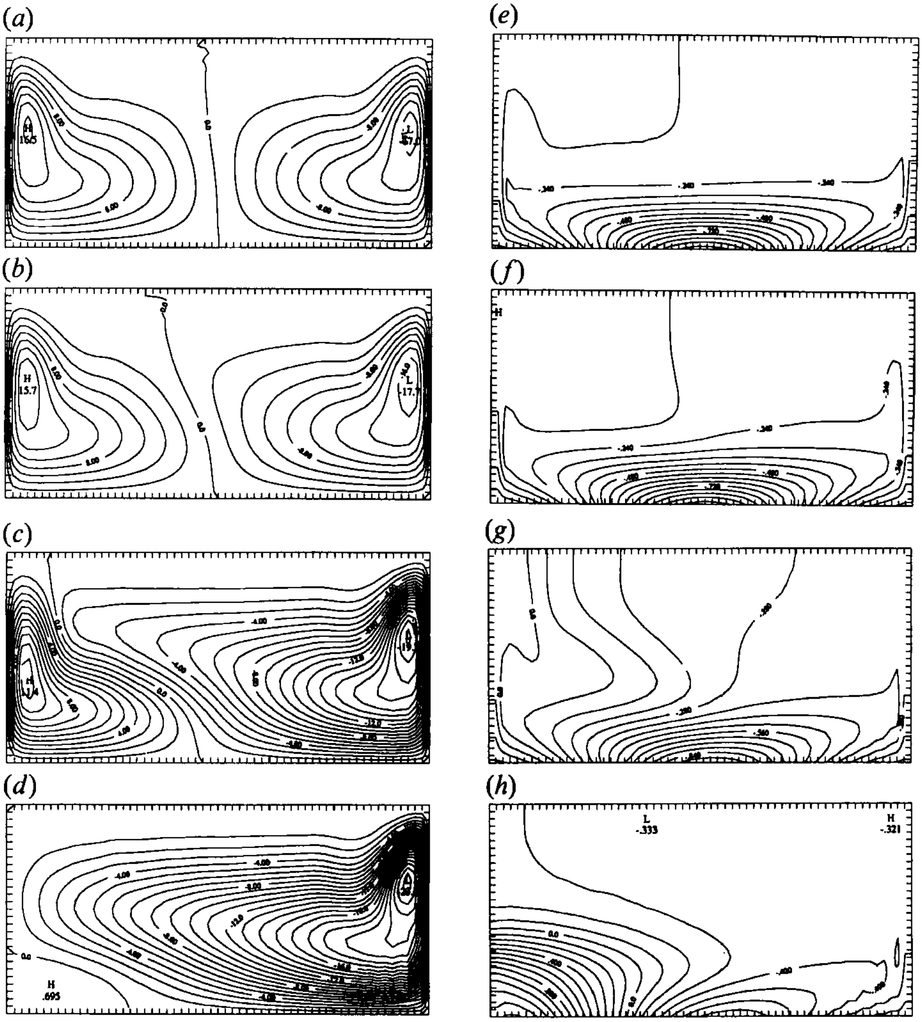

FIGURE 13. The time evolution of the stream function and salinity over the growth period shown in figure 12. (*a*–*d*) The stream function at time steps 36, 39, 42 and 54 k; (*e*–*h*) the salinity at the corresponding timesteps. Contour intervals are 2.00 for ψ and 0.06 for salinity in (*e*) and (*f*), 0.07 in (*g*) and 0.10 in (*h*).

5. Neutral stability curve and physical bifurcation mechanism

We have shown that at different values of γ and Ra, the symmetric state can bifurcate into one of two asymmetric states. We shall now summarize the results in a γ-Ra regime diagram for this bifurcation. As we have indicated earlier in the paper, because of the large number of free parameters, we are not able to explore the neutral stability surface in the complete multi-dimensional parameter space Ω of (2.8). The curve presented in figure 14 is for $\eta = 1$, $\sigma = 2.25$, $\lambda = 0.32$, and $d = 0.2$.

This curve is defined by a number of discrete points over 3 decades of Rayleigh number, and for $\gamma \leqslant 1.4$. There appear to be two orthogonal asymptotes that this curve may approach, respectively at $\gamma \approx 0.3$ and $Ra \approx 10^5$. At the high-Ra end of the curve, the requirements for grid resolution and computational timestep are very stringent in order to maintain computational stability and to attain acceptable

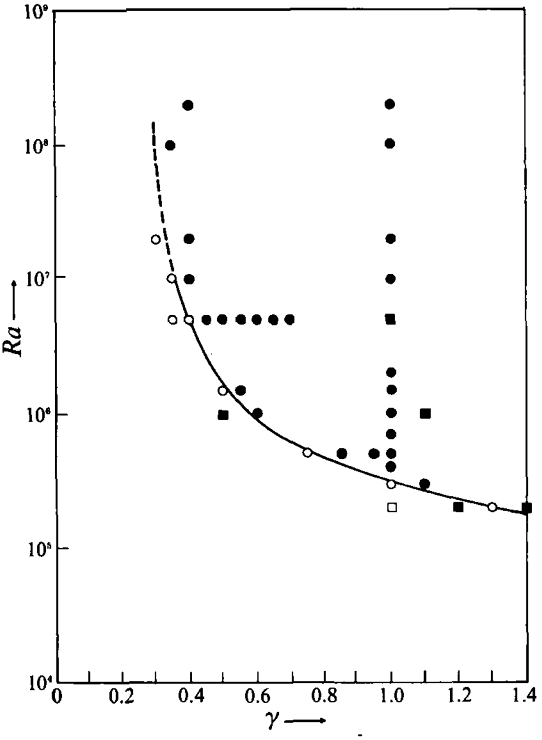

FIGURE 14. The stability curve in the γ-Ra plane. The solid symbols represent asymmetric states and the open symbols symmetric ones. The circles are for $d = 0.2$ and the few squares are for $d = 1.0$. All cases are for $\eta = 1$, $\sigma = 2.25$ and $\lambda = 0.32$.

numerical accuracy. We have not been able to determine the position of the curve above $Ra = 5 \times 10^6$ as accurately as below it; more refined computations would sharpen and extend our results in this part of the regime diagram.

In figure 14, we have also incorporated a few points for aspect ratio unity. Most of these points indicate, not surprisingly, asymmetric flows. Indeed, if we use the vertical dimension of the container to define the Rayleigh number, and if we conceptually accept that – at higher Rayleigh numbers – smaller values of γ are required for bifurcation, then the curve for $d = 1.0$ would shift to the left of the curve for $d = 0.2$. Consequently, most of the points for $d = 1.0$ presented here would fall on the asymmetric side of the curve as shown; we have not completely traced the appropriate curve for $d = 1.0$, which seems of lesser geophysical interest.

In order to understand, at least qualitatively, the broad implication of the stability curve, we retrace the physical arguments some previous workers have used to explain the instability of the symmetric circulation. Following Marotzke *et al.* (1988), we start with a symmetric basic state. Let us assume that a parcel of fluid near the bottom, with a given heat and salt content, is perturbed, and that this perturbation will increase the parcel's buoyancy. Consequently the parcel will rise, and other fluid parcels will move in to replace it. When the restoring boundary condition is used, the fixed boundary value of salt at the bottom will be able to maintain the ambient salinity constant. When the parcels return to their original positions, they will be 'restored' to the ambient salinity. Hence the perturbed parcels will be stabilized.

However, if the salt-flux condition is applied while the symmetric state is

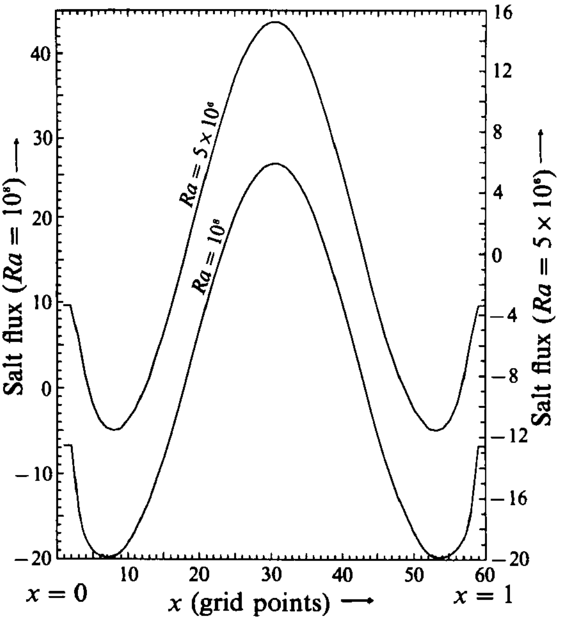

FIGURE 15. The salt flux across the bottom boundary computed from the symmetric solutions for $Ra = 5\times10^6$ and $Ra = 10^8$; $d = 0.2$. Note the shift in vertical scales.

perturbed, the sequence of events can be very different. First, let us assume the perturbed parcels are situated near the lower right-hand corner, and neglect the diffusive loss or gain of buoyancy in their paths. Since the perturbation makes the parcels more buoyant and hence causes them to go faster, they will complete the flow circuit in a shorter time than the unperturbed parcels. After they return to the boundary, their salt content will not be restored to their original state; instead they will lose more salt because of the negative salt-flux condition. Consequently, the particles will gain speed over each complete circuit of the perturbed cell. The salt-flux boundary condition therefore creates a positive feedback in particle speed. This continuous increase in speed will cause instability; it will also favour asymmetry, since the assumed perturbation is not symmetric, nor will natural perturbations ever be perfectly symmetric. This is the essence of Marotzke *et al.*'s mechanism for the bifurcation.

The mechanism just described can be used to understand one aspect of our stability curve, namely that as Ra increases, a smaller γ is required for instability. There are two factors involved here. First, the non-dimensional salt flux is larger at higher Rayleigh number because of the difference in the flow structures. Figure 15 shows the vertical salinity gradient for $Ra = 10^8$ and 5×10^6 across the bottom boundary. Comparison of figure 5(a, b) with figure 6(a, b) shows that the isotherms and isohalines are packed closer to the bottom at higher Rayleigh numbers. This compactness increases the vertical gradient of all fields near the boundary.

Secondly, the strength of the concentrate is proportional to λRa. Thus at higher Rayleigh number with λ held constant, the effective salt flux increases because it is proportional to $\lambda Ra(\partial S/\partial z)$. The feedback mechanism is more efficient for higher Ra because that implies a large salt flux, both in terms of Ra itself and in terms of $\partial S/\partial z$. The fact that indeed the higher Ra, the lower is the critical value for γ, supports the heuristic argument of a salt-flux feedback mechanism. The explanation of other aspects of the curve in figure 14, namely of the apparent vertical and horizontal asymptotes, should help us understand better the bifurcation mechanism in the future.

6. Conclusions and further work

6.1. *Summary*

We have studied thermosolutal convection for two-dimensional flows governed by the Navier–Stokes equations with the Boussinesq approximation, coupled to the full transport equations for heat and salt. Our results show that, when prescribing both temperature T and salinity S on the boundary symmetrically about the central vertical axis of the rectangular box containing the flow, a two-cell circulation with the same symmetry is the unique, stable solution. For convenience and compatibility with the earlier work of the lead author (Quon 1987), the inhomogeneous boundary conditions were imposed at the bottom, rather than the top boundary. Thus to compare directly the present results with those of previous authors and with oceanic circulation, all flow patterns have to be reflected in a horizontal axis through the centre of the box.

We have confirmed that, when the prescribed salinity, called 'restoring' boundary condition by previous authors, is replaced by a salt-flux condition obtained by diagnosing this flux from the prescribed T- and S-solution, the symmetric solution becomes unstable. The solutions which become unstable for such mixed boundary conditions, restoring T but diagnosing the salt flux, are pairwise asymmetric, each having a mirror image in the central vertical axis: one has a dominant cell on the left, the other on the right. The emergence of one or the other asymmetric solution seems to be favoured by perturbing the symmetric flow, in the presence of mixed boundary conditions, within that half of the box where the cell is to grow.

The transfer of stability from a single equilibrium to a pair of equilibria with mirror symmetry suggests the presence of a *pitchfork bifurcation* in the system. An important result of this study is that, in fact, the asymmetric states are not necessarily one-cell states, as suggested by some of the earlier work on the ocean's thermohaline circulation (Bryan 1986; Marotzke *et al.* 1988), but that the dominant cell grows gradually away from the bifurcation point. At the high Rayleigh numbers Ra and very low aspect ratios $d = H/L$ considered by most of the above-cited authors, owing to their concern for oceanic verisimilitude, one-cell circulations do seem to be much more likely, the transitional Ra-range of coexistence between one large and one small cell being at lower values of Ra for such d. It is noteworthy, however, that the present-day circulation of the Atlantic Ocean (Fuglister 1960; Defant 1961) has in fact two very unequal cells, with North Atlantic Deep Water (NADW) forming in the Norwegian and Labrador Seas and flowing across the equator to rise again at the Antarctic Circumpolar Front, while Antarctic Bottom Water (AABW) forms in the Weddell Sea, flows northward through the South Atlantic under NADW and returns to rise with it along the same polar front.

As in most fluid-dynamical problems, there are many non-dimensional parameters which affect the flow qualitatively, or at least quantitatively. Among these, the most important ones are Ra, d, the Lewis number η (the ratio of salt and heat diffusivities), the Prandtl number σ, and the salt-flux strength on the boundary γ (see equations (2.7), (2.8)). Of the six parameters in (2.8), the two which are essential to the bifurcation are Ra and γ. We have explored changes in Ra by five orders of magnitude and in γ by one order.

A neutral stability curve in the Ra-γ plane (figure 14) separates the domain of stability of symmetric states from that of asymmetric ones. Bifurcation of the pairwise asymmetric states from the symmetric ones follows by traversing this curve at any point, whether increasing Ra, γ, or both. Intuitively, it is clear that the system is stressed further by either increase, and therewith, as in many other physical, chemical and biological systems, that the symmetry decreases as the stress increases. The gradual increase of the degree of asymmetry away from the bifurcation point(s) is shown in figures 8 and 9.

The effect of changes in three additional parameters, d, σ and η, each by about an order of magnitude, was also studied. A change in Prandtl number σ from $\sigma = 2.25$, used for convenience in most of the computations, to $\sigma = 7.1$, the correct value for water, showed very little change in the solutions. The change in Lewis number η from $\eta = 1.0$, used for convenience in most of the computations, to the more realistic value of $\eta = 0.10$ (figure 11), is equivalent to an increase in Ra as far as tighter packing of isohalines close to the boundaries is concerned.

The exploratory use of aspect ratio $d = 1.0$, rather than the more realistic $d = 0.2$ used otherwise, shows that it corresponds to a lowering of the neutral stability curve in the γ-Ra plane (figure 14). Most of the flow in the more highly stressed situations at unit aspect ratio (figures 4, 5 and 6) still occurs in the lower, forced part of the container. While high aspect ratios, $d = O(1)$ and higher, are not of primary interest for the oceanic application motivating the present study, a more thorough exploration of the effect of d, from $d = O(10^{-2})$ to $d = O(10)$, seems worthwhile from the broader perspective of fluid dynamics.

Following earlier theoretical investigations, we have not included here the effects of rotation. OGCM (Bryan 1986) and coupled GCM (Manabe & Stouffer 1988) experiments suggest that the symmetry breaking of the ocean's thermohaline circulation does occur in the presence of rotation as well. We expect to pursue systematically the effect of Coriolis forces in an idealized two-dimensional system similar to the present one.

The general shape of the stability curve in figure 14 supports the physical mechanism of the salt-flux instability proposed by Marotzke *et al.* (1988): once the salt content of a fluid parcel near the boundary is perturbed, that content, after a circuit in the flow cell to which the parcel belongs, will be restored by an imposed-salinity condition, but will be further modified – under appropriate circumstances – by a salt-flux condition, thus accelerating the parcel and increasing therewith the size of the cell to which it belongs. This mechanism is supported by the fact that, as Ra increases, a smaller γ is required – in our numerical experiments – for instability. But the appearance of a limiting γ-value, $\gamma \approx 0.3$, for high Ra, and of a limiting Ra-value, $Ra \approx 10^5$, for high γ, seems to be a nonlinear effect not explained by this linear instability argument, and worthy of further investigation.

6.2. *Discussion*

While the idealized model studied here is far from the complexity of the oceans' thermohaline circulations, past, present and future, certain analogies between our results so far, on the one hand, and documented or suspected features of these circulations, on the other, are too suggestive not to mention, at least in passing.

The present circulation of the Atlantic is temperature-dominated and asymmetric, with deep waters forming near the poles and the northern cell dominating the southern one. Salinity-dominated circulations (Stommel 1961) however, are suspected to have occurred at peak glaciation, when the subpolar seas were completely ice covered and no deep water could form there, as well as during much warmer climates such as the Cretaceous, when no substantial cooling occurred near the poles (Weyl 1968). In both cases, the densest waters available for sinking were at low latitudes, owing to enhanced evaporation, such as in today's Mediterranean Sea. Recent evidence for a salinity-dominated (halothermal) circulation during the Eocene (58–36 million years ago) and for a mixed, salinity- and temperature-dominated (halothermal and thermohaline) circulation during the Oligocene (36–23 million years ago) has been adduced by Kennett & Stott (1990, 1991).

The thermohaline circulation in today's Pacific Ocean is largely driven by that of the Atlantic, to which it is connected by the Antarctic Circumpolar Current. It has one cell, with deep waters travelling northward, rising and returning southward. Deep-water formation in the North Pacific has been hypothesized for different times in the past, although not conclusively documented by deep-sea core studies. On the other hand, enhancement of deep-water formation near Antarctica, to the detriment of NADW formation (Boyle & Keigwin 1987), has been shown to have occurred during certain phases of the last complete glacial cycle (150000 years ago until now), along with a marked northward expansion of the Atlantic's southern cell (Duplessy *et al.* 1988).

A particularly intriguing aspect, in this perspective, of our results is the systematic exploration of the salt-flux intensity γ, as it affects the thermohaline circulation. The excess salinity of the North Atlantic compared to the World Ocean, and the comparable salinity defect of the North Pacific have suggested to chemical oceanographers (Schnitker 1982; Broecker & Denton 1989) that changes in the atmosphere's hydrologic cycle might affect substantially the ocean circulation, and vice versa. These ideas have been illustrated recently with preliminary numerical results by Wright & Stocker (1991), and could be tested more completely by an extension of our γ-Ra bifurcation results to a more realistic ocean model, coupled to a minimal atmospheric model. Such an extension is being contemplated by the present authors, with their colleagues at UCLA.

It is a pleasure to thank our colleagues Yizhak Feliks, Fei-fei Jin, and David Neelin for stimulating discussions during the course of this work. C.Q. also wishes to thank all members of the Department of Atmospheric Sciences at UCLA who have made his sabbatical visit so very enjoyable. Similarly, M.G. would like to thank the members of the Laboratoire de Mètèrologie Dynamique du CNRS, Ecole Normale Supèrieuse, F-75231, Paris, France for their hospitality during both a sabbatical and regular shorter visits. At the time of preparation of this manuscript, Olivier Thual and James C. McWilliams kindly provided us with a pre-publication copy of their closely related paper, and with useful comments on ours. Preprints of Weaver & Sarachik (1991) and of Wright & Stocker (1991) were also provided by Andrew J. Weaver. This work was supported by ONR Grant N00014-89-J-1845, DOE Grant W/GEC0014 (through the National Institute for Global Environmental Change, NIGEC), and a Guggenheim Fellowship to M.G.

Appendix A. Analytical results for low *Ra*

The approximate analytical treatment given in Appendices A and B is meant to help understand some of the computational results, which are much more accurate and complete. Equations (2.3) and (2.4) for T and S are equivalent if we consider

$\eta = 1$. The solutions are the same if we apply the same boundary conditions. Therefore, in order to obtain quasi-steady symmetric solutions, we need to solve (2.1)–(2.3), and (2.5), with $Ra(T-\lambda S)$ replaced by ΛRaT, $\Lambda = 1-\lambda$.

For low Rayleigh number flows, $Ra \to 0$, it is more appropriate to scale the stream function by κRa (Batchelor 1954). If we expand T, the temperature, and ψ, the stream function, in powers of Ra, the lowest-order equations are:

$$\nabla^2 T = 0, \tag{A 1}$$

$$\nabla^4 \psi = -\Lambda \cdot T_x, \tag{A 2}$$

where $-\partial\psi/\partial z = u$, and $\partial\psi/\partial x = w$. The boundary conditions are (2.6*a–e*).

(A 1) is the heat diffusion equation for which we can obtain an exact solution with boundary conditions (2.6*d, e*). In order to satisfy $\partial T/\partial x = 0$ at $x = 0, 1$, we shall represent T by a Fourier cosine series:

$$T(x,z) = \sum_{n=0}^{\infty} f_n(z)\cos(n\pi x). \tag{A 3}$$

Substituting (A 3) into (A 1) we get

$$\partial^2 f_n(z)/\partial z^2 - (n\pi)^2 f_n(z) = 0. \tag{A 4}$$

The solution of (A 4) is

$$f_n(z) = a_n\, \mathrm{e}^{n\pi z} + b_n\, \mathrm{e}^{-n\pi z}, \tag{A 5}$$

$$T(x,z) = \sum_{n=0}^{\infty} \cos(n\pi x)(a_n\, \mathrm{e}^{n\pi z} + b_n\, \mathrm{e}^{-n\pi z}). \tag{A 6}$$

In order to satisfy boundary condition (2.6*e*) at $z = 0$, we require

$$(a_0+b_0) = -\tfrac{1}{2}, \quad (a_2+b_2) = \tfrac{1}{2}, \quad a_n = b_n = 0 \quad \text{for } n \neq 0 \text{ or } 2;$$

after applying (2.6*d*) at $z = d$, we have

$$a_2 = b_2\, \mathrm{e}^{-4\pi d} = \tfrac{1}{2} - b_2, \quad b_2 = \tfrac{1}{4}.$$

Hence,

$$T(x,z) = \frac{1}{2}\left(\cos 2\pi x \frac{\cosh 2\pi(d-z)}{\cosh 2\pi d} - 1\right), \tag{A 7}$$

with (A 7) satisfying all boundary conditions in (2.6*d*) and (2.6*e*). When we substitute (A 7) into the right-hand side of (A 2), we have

$$\nabla^4 \psi = \Lambda\pi \sin 2\pi x \frac{\cosh 2\pi(d-z)}{\cosh 2\pi d}. \tag{A 8}$$

Let us assume (A 8) has a solution of the form

$$\psi = \frac{\Lambda\pi}{\cosh 2\pi d} \sin 2\pi x\, Y(z), \tag{A 9}$$

where $Y(z)$ satisfies the equation:

$$Y_{zzzz}(z) - 2(2\pi)^2\, Y_{zz}(z) + (2\pi)^4\, Y(z) = \cosh 2\pi(d-z). \tag{A 10}$$

In order to satisfy the boundary conditions, let Y be of the form

$$Y(z) = \sum_{n=1}^{\infty} p_n \sin(n\pi z/d). \tag{A 11}$$

If we also expand $\cosh 2\pi(d-z)$ in a sine series as

$$\cosh 2\pi(d-z) = \sum_{n=1}^{\infty} q_n \sin(n\pi z/d), \tag{A 12}$$

where
$$q_n = (2/d)\int_0^d \cosh 2\pi(d-z)\sin(n\pi z/d)\,\mathrm{d}z$$

$$= \frac{2n}{4d^2+n^2}\{\cosh 2\pi d + (-1)^{n+1}\}, \tag{A 13}$$

(A 12) is valid over the whole range of z except at the boundary points, where the right-hand side of (A 8) is not required. If we substitute (A 12) and (A 13) into (A 10), and solve the resulting equations for each individual Fourier component, we obtain

$$p_n = \frac{d^4}{\pi^4(n^2+4a^2)^2}q_n,$$

yielding

$$Y(z) = \sum_{n=1}^{\infty} \frac{2nd^4}{\pi^5(4d^2+n^2)^3}\{\cosh 2\pi d + (-1)^{n+1}\}\sin(n\pi z/d). \tag{A 14}$$

The complete solution is

$$\psi(x,z) = \frac{A\pi}{\cosh 2\pi d}\sin(2\pi x)\,Y(z). \tag{A 15}$$

The stream function $\psi(x,z)$ in (A 15) satisfies all the required boundary conditions, i.e. $\psi(x,z) = 0$ at $x = 0, 1$, $z = 0$, d, $\psi_{xx} = 0$ at $x = 0, 1$, and $\psi_{zz} = 0$ at $z = 0$.

The z-structure of (A 15) is difficult to visualize from the infinite series (A 11) for $Y(z)$. Noting, however, that the coefficients of $\sin(n\pi z)$ in (A 14) are inversely proportional to n^5, we approximate (A 15) by its first term,

$$\psi(x,z) \approx \frac{2Ad^4}{\pi^4(4d^2+1)^3}\left(1+\frac{1}{\cosh 2\pi d}\right)\sin(2\pi x)\sin(\pi z/d). \tag{A 16}$$

This approximate solution represents a two-cell circulation. If we include the second term in (A 14), which has less than $\frac{1}{32}$ of the amplitude of the first term, the cells will become slightly askew towards the bottom. This is in fact a distinct characteristic of the two cells in the symmetric states for Ra as high as 10^6 and $d = 0.2$ (figure 4).

Obviously, the salinity distribution is the same as the temperature distribution (A 7),

$$S(x,z) = \tfrac{1}{2}\cos 2\pi x\left\{\frac{\cosh 2\pi(d-z)}{\cosh 2\pi d} - 1\right\}, \tag{A 17}$$

which also satisfies the following boundary condition at $z = 0$

$$\partial S/\partial z = -\pi\cos 2\pi x \tanh 2\pi d = f(x). \tag{A 18}$$

Note that as $d \to \infty$, T and S approach uniform temperature and salinity values of $-\frac{1}{2}$ at $z = d$, which is the boundary value at $z = 0$, a quarter of the way from either side boundary (see figure 4c).

Now if we use $\gamma f(x)$, with $f(x)$ being given by (A 18), as the boundary condition for the salt equation, the solution for the temperature remains the same, (A 7), but the solution for salt is changed by a factor of γ. The solution for ψ is still given by (A 15), except now $\Lambda = 1-\gamma\lambda$. This holds for λ greater or smaller than unity, and also for positive or negative values of γ, as long as ΛRa remains small.

Appendix B. Analytical results at high *Ra*

At high Reynolds number, $Ra \rightarrow \infty$ we shall scale the stream function ψ by κ_T. We obtain the following equations (Gill 1966):

$$\nabla^4\psi + \Lambda Ra\, T_x = (1/\sigma)\, J(\psi, \nabla^2\psi), \tag{B 1}$$

$$\nabla^2 T = J(\psi, T). \tag{B 2}$$

For $\sigma \rightarrow \infty$, which can be assumed for water with $\sigma = 7.1$, the right-hand side of (B 1) can be dropped, but (B 2) is still nonlinear.

B.1. *The interior solutions*

In the interior of the enclosure, we shall assume that the solution is smooth. For sufficiently large Rayleigh number, (B 1) can be approximated by

$$T_x = 0.$$

Hence
$$T = T(z).$$

Substituting (B 2) into (B 1), and assuming ψ to be antisymmetric about $x = \frac{1}{2}$, we have

$$\psi(x,z) = (T_{zz}/T_z)(x-\tfrac{1}{2}). \tag{B 3}$$

The interesting feature of (B 3) is that if $T(z) = \mathrm{e}^{-az}$, then $\psi = a(x-\frac{1}{2})$, which is independent of z and is a linear function of x. It has been observed above in §4.2.1 (ii) that this is in fact a distinct characteristic of the high-*Ra* flow. Of course, these solutions do not satisfy the respective boundary conditions, for which we need boundary layers along all the boundaries.

At extremely high Rayleigh number, the flow may become so strong that the nonlinear term in (B 1) is no longer negligible. In that case, even if $T_x = 0$ in the interior, ψ is governed by a nonlinear elliptic equation. The solution shown in figure 6(*d*) for $Ra = 10^8$ is a good example. Since (B 2) is nonlinear at sufficiently high Rayleigh number and it is difficult to obtain even an approximate solution for it (see Gill 1966), we make only some order-of-magnitude estimates for the boundary scales here.

B.2. *Approximate sidewall boundary-layer scale*

In order to gain some insight into the boundary-layer flows, we linearize near the boundary by using average values denoted by superscript (0). Near the sidewalls, the terms containing the x-derivatives become important. We consider the following approximate equations:

$$\psi_{xxxx} = -\Lambda Ra\, T_x, \tag{B 4a}$$

$$T_{xx} = T_z^{(0)}\, \psi_x + u^{(0)} T_x. \tag{B 4b}$$

The second term on the right-hand side of (B 4*b*) can be dropped if $u^{(0)}$ is small. After eliminating T and using a stretched coordinate $\nu = Ra^{\frac{1}{4}}x$, we have

$$\psi_{\nu\nu\nu\nu} = -\Lambda T_z^{(0)}\, \psi. \tag{B 5}$$

The sidewall boundary layer scale is therefore $Ra^{-\frac{1}{4}}$.

B.3. *Approximate bottom boundary-layer scale*

By the argument that $\psi_z \gg \psi_x$, which is small in the bottom boundary layer, we have

$$\psi_{zzzz} + A\,Ra\,T_x = 0,$$
$$T_{zz} + T_x^{(0)}\,\psi_z - w^{(0)} T_z = 0.$$

If we eliminate ψ we obtain

$$T_{zzzzz} - A\,Ra\,T_x^{(0)}\,T_x - w^{(0)} T_{zzzz} = 0. \qquad \text{(B 6)}$$

Now if we use a stretched coordinate $\mu = Ra^{\frac{1}{5}} z$, then (B 6) becomes

$$T_{\mu\mu\mu\mu\mu} - A T_x^{(0)}\,T_x - w^{(0)} Ra^{-\frac{1}{5}} T_{\mu\mu\mu\mu} = 0. \qquad \text{(B 7)}$$

The last term in (B 7) drops out if we assume $Ra^{\frac{1}{5}} \gg w^{(0)}$. The horizontal boundary-layer scale is therefore $O(Ra^{-\frac{1}{5}})$, which is larger than the vertical boundary-layer scale of $Ra^{-\frac{1}{4}}$.

The sidewall and bottom boundary-layer structures obtained numerically in figure 7 seem to confirm the arguments presented here.

Appendix C. Bifurcation diagram

It is difficult to determine analytically the stability curve drawn approximately in figure 14, because eigenvalues have to be computed for a linearization of the governing equations (2.1)–(2.7) about a non-trivial basic state, and the dependence on the parameters (2.8) is highly implicit and nonlinear. In this Appendix we use the numerical results for Rayleigh number $Ra = 5 \times 10^6$ as a function of γ to construct a bifurcation diagram by nonlinear regression. The bifurcation point of this diagram provides an approximation to the critical value of γ for $Ra = 5 \times 10^6$ in figure 14.

Assuming pitchfork bifurcation as explained in §1 (see also Thual & McWilliams 1992), we formally fit the data to the following model (Guckenheimer & Holmes 1983):

$$A_0(\phi - \phi_0)^2 = \gamma - \gamma_0, \qquad \text{(C 1)}$$

where ϕ can be any of the dynamical variables in the system, e.g. the maximum value of the stream function in the rectangle. Equation (C 1) describes a parabola whose axis is represented by the line $\phi = \phi_0$ and whose apex is at the bifurcation point (γ_0, ϕ_0). Given Ra and the other parameters in (2.8) fixed, the symmetric steady state loses its stability to either one of the two asymmetric states as γ increases through the value γ_0. A_0 is a scaling factor that defines a family of curves with the same apex and the same axis of symmetry.

We have used three different functionals of the stream function, ψ, defined below to represent ϕ in equation (C 1):

$$\phi_1 = \left(\int_x \int_z (\psi - \psi_a)^2 \,\mathrm{d}x\,\mathrm{d}z \right)^{\frac{1}{2}}, \qquad \text{(C 2a)}$$

$$\phi_2 = |\psi_{\max} + \psi_{\min}|, \qquad \text{(C 2b)}$$

$$\phi_3 = |\psi_{a,\max}|, \qquad \text{(C 2c)}$$

where ψ_a is defined as

$$\psi_a(x, z) = \tfrac{1}{2}\{\psi(x, z) + \psi(-x, z)\}. \qquad \text{(C 2d)}$$

The results of seven separate numerical experiments, for $\gamma = 0.40$, 0.425, 0.45, 0.50, 0.55, 0.60, and 0.65 respectively, are used in the regression. All of them have

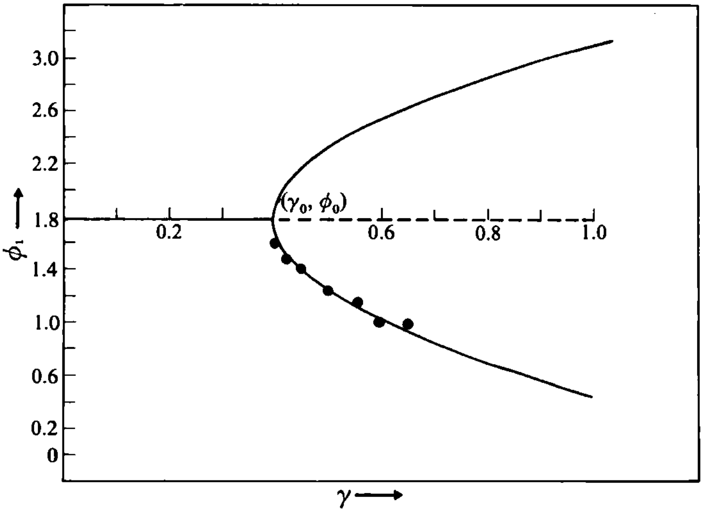

FIGURE 16. A pitchfork bifurcation diagram fitted by nonlinear regression to seven points obtained numerically (compare figure 14, $Ra = 5 \times 10^6$). The dots represent the experimental values of ϕ_1 defined by equation (C 2*a*).

definite asymmetric circulations except the one for $\gamma = 0.40$ which is symmetric. The three critical values of γ_0 are found to be $\gamma_0^{(1)} = 0.3962$, $\gamma_0^{(2)} = 0.4023$, and $\gamma_0^{(3)} = 0.4033$. The average value is 0.4006. An estimate of γ_0 from figure 14 is in the neighbourhood of 0.40.

Figure 16 gives the regression curve for ϕ_1 *vs.* γ with the seven experimental values of ϕ_1 shown as black dots. Both ϕ_2 and ϕ_3 yield very similar curves.

REFERENCES

ARAKAWA, A. & LAMB, V. 1977 Computational design of the basic dynamical processes of the UCLA general circulation model. *Meth. Comput. Phys.* **17**, 173–265.

BARENBLATT, G. I. 1979 *Similarity, Self-similarity, and Intermediate Asymptotics.* New York, London: Publishing Consultants Bureau.

BATCHELOR, G. K. 1954 Heat transfer by free convection across a closed cavity between vertical boundaries at different temperatures. *Q. Appl. Maths* **12**, 209–233.

BOYLE, E. A. & KEIGWIN, L. 1987 North Atlantic thermohaline circulation during the past 20,000 years linked to high-latitude surface temperature. *Nature* **330**, 35–40.

BROECKER, W. S. & DENTON, G. H. 1989 The role of ocean-atmosphere reorganizations in glacial cycles. *Geochim. Cosmochim Acta* **53**, 2465–2501.

BROECKER, W. S., PETEET, D. M. & RIND, D. 1985 Does the ocean–atmosphere system have more than one stable mode of operation? *Nature* **315**, 21–25.

BUSSE, F. 1978 Nonlinear properties of thermal convection. *Rep. Prog. Phys.* **41**, 1929–1967.

BRYAN, F. 1986 High-latitude salinity effects and interhemispheric thermohaline circulation. *Nature* **323**, 301–304.

CHORIN, A. J. 1968 Numerical solution of the Navier–Stokes equations. *Maths Comput.* **22**, 745–762.

CHORIN, A. J. 1969 On the convergence of discrete approximations to the Navier–Stokes equations. *Maths Comput.* **23**, 341–353.

DANIELS, P. G. & STEWARTSON, K. 1977 On the spatial oscillations of a horizontally heated rotating fluid. *Math. Proc. Camb. Phil. Soc.* **81**, 325–349.

DANIELS, P. G. & STEWARTSON, K. 1978 On the spatial oscillations of a horizontally heated rotating fluid II. *Q. J. Mech. Appl. Maths* **31**, 113–135.

Defant, A. 1961 *Physical Oceanography*, vol. 1. Pergamon.

Duplessy, J.-C. & Shackleton, N. J. 1985 Response of global deep-water circulation to Earth's climatic change 135,000–107,000 years ago. *Nature* **316**, 500–507.

Duplessy, J.-C., Shackleton, N. J., Fairbanks, R. G., Labeyrie, L., Oppo, D. & Kallel, N. 1988 Deepwater source variations during the last climatic cycle and their impact on the global deepwater circulation. *Paleoceanography* **3**, 343–360.

Fuglister, F. C. 1960 Atlantic Ocean atlas of temperature and salinity profiles and data from the International Geophysical Year of 1957–1958. Woods Hole Oceanographic Institution, MA, USA. 209 pp.

Ghil, M. & Childress, S. 1987 *Topics in Geophysical Fluid Dynamics: Atmospheric Dynamics, Dynamo Theory and Climate Dynamics*. Springer. 485 pp.

Ghil, M., Mullhaupt, A. & Pestiaux, P. 1987 Deep water formation and Quaternary glaciations. *Climate dyn.* **2**, 1–10.

Ghil, M. & Vautard, R. 1991 Interdecadal oscillations and the warming trend in global temperature time series. *Nature* **350**, 324–327.

Gill, A. E. 1966 The boundary layer regime for convection in a rectangular cavity. *J. Fluid Mech.* **26**, 515–536.

Guckenheimer, J. & Holmes, P. 1983 *Nonlinear Oscillations, Dynamical Systems, and Bifurcations of Vector Fields*. Springer. 453 pp.

Kagan, B. A. & Maslova, N. B. 1990 Multiple equilibria of the thermohaline circulation in a ventilated ocean model. Ocean Modelling, issue 90. (Unpublished manuscript obtainable from: Hooke Institute, Oxford University.)

Kennett, J. P. & Stott, L. D. 1990 Proteus and Proto-Oceanus: ancestral Paleogene oceans as revealed from antarctic stable isotopic results ODP LEG 113. *Proceedings of the Ocean Drilling Program. Scientific Results*, vol. 113, pp. 865–880.

Kennett, R. P. & Stott, L. D. 1991 Abrupt deep-sea warming, palaeoceanographic changes and benthic extinctions at the end of the palaeocene. *Nature* **353**, 225–229.

Krishnamurti, R. 1973 Some further studies on transition to turbulent convection. *J. Fluid Mech.* **60**, 285–303.

Lohmann, G. P. 1978 Response of deep sea to ice ages. *Oceanus* **21**, 58–64.

McIntyre, M. E. 1968 The axisymmetric convective regime for a rigidly bounded rotating annulus. *J. Fluid Mech.* **32**, 625–655.

Maier-Reimer, E. & Mikolajewicz 1989 Experiments with an OGCM on the cause of the Younger Dryas. *Oceanography* 87-100, (ed. A. Ayala-Castanares, W. Wooester, A. Yanez-Arancibia).

Manabe, S. & Stouffer, R. J. 1988 Two stable equilibria of a coupled ocean atmosphere model. *J. Climate* **1**, 841–866.

Marotzke, J., Welander, P. & Willebrand, J. 1988 Instability and multiple steady states in a meridional-plan model of the thermohaline circulation. *Tellus* **40**A, 162–149.

Quon, C. 1972 High Rayleigh number convection in an enclosure – a numerical study. *Phys. Fluids* **15**, 12–19.

Quon, C. 1976 A mixed spectral and finite difference model to study baroclinic annulus waves. *J. Comput. Phys.* **29**, 442–479.

Quon, C. 1980 Quasi-steady symmetric regimes of a rotating annulus differentially heated on the horizontal boundaries. *J. Atmos. Sci.* **37**, 2407–2423.

Quon, C. 1983 Effect of grid distribution on the computation of high Rayleigh number convection in a differentially heated cavity. In *Numerical Properties and Methodologies in Heat Transfer* (ed. T. M. Shih), pp. 261–281. Hemisphere and Springer.

Quon, C. 1987 Nonlinear response of a rotating fluid to differential heating from below. *J. Fluid Mech.* **181**, 233–263.

Rooth, C. 1982 Hydrology and ocean circulation. *Prog. Oceanogr.* **11**, 131–149.

Schnitker, D. 1982 Climatic variability and deep ocean circulation: evidence from the Northern Atlantic. *Paleogeogr.* **40**, 213–234.

Shackleton, N. J., Duplessy, J.-C., Arnold, M., Maurice, P., Hall, M. A. & Cartlidge, J. 1988 Radiocarbon age of last glacial Pacific deep water. *Nature* **335**, 708–710.

STOMMEL, H. M. 1961 Thermohaline convection with two stable regimes of flow. *Tellus* XIII **2**, 224–230.

THUAL, O. & MCWILLIAMS, J. C. 1992 The catastrophe structure of thermohaline convection in a two-dimensional fluid model and a comparison with low-order box model. *J. Geophys. Astrophys. Fluid Dyn.* **64**, 67–95.

TURNER, J. S. 1973 *Buoyancy Effects on Fluids.* Cambridge University Press.

VARGA, R. S. 1962 *Matrix Iterative Analysis.* Prentice-Hall.

WEAVER, A. J. & SARACHIK, E. S. 1991 The role of mixed boundary conditions in numerical models of the ocean's climate. *J. Phys. Oceanogr.* **21**, 1470–1493.

WELANDER, P. 1986 Thermohaline effects in the ocean circulation and related simple models. In *Large-scale Transport Processes in Oceans and Atmosphere* (ed. J. Willebrand & D. T. L. Anderson), pp. 163–200. D. Reidel.

WEYL, P. K. 1968 The role of the oceans in climatic change: A theory of the ice ages. *Meteorol. Monogr.* **8**(30), 37–62.

WRIGHT, D. G. & STOCKER, T. F. 1991 A zonally averaged ocean model for the thermohaline circulation. Part I: Model development and flow dynamics. *J. Phys. Oceanogr.* **21**, 1713–1724.